The NO_x-HNO_3 System in the Lower Stratosphere: Insights from In Situ Measurements and Implications of the J_{HNO_3}−[OH] Relationship◇

K. K. Perkins,*,† T. F. Hanisco,† R. C. Cohen,‡ L. C. Koch,‡,§ R. M. Stimpfle,† P. B. Voss,† G. P. Bonne,†,|| E. J. Lanzendorf,† J. G. Anderson,† P. O. Wennberg,⊥ R. S. Gao,⊗ L. A. Del Negro,⊗,▽ R. J. Salawitch,# C. T. McElroy,@ E. J. Hintsa,†,¶ M. Loewenstein,£ and T. P. Bui£

Department of Chemistry and Chemical Biology, Harvard University, Cambridge, Massachusetts 02138; Departments of Chemistry and of Geology and Geophysics, University of California, Berkeley, California 94720; Divisions of Engineering and of Geological and Planetary Science, California Institute of Technology, Pasadena, California 91125; NOAA Aeronomy Laboratory, Boulder, Colorado 80303; NASA Jet Propulsion Laboratory, California Institute of Technology, Pasadena, California 91109; Meteorological Service of Canada, Environment Canada, Downsview, Ontario, Canada; and NASA Ames Research Center, Moffett Field, California 94035

Received: July 14, 2000; In Final Form: November 2, 2000

During the 1997 Photochemistry of Ozone Loss in the Arctic Region in Summer (POLARIS) mission, simultaneous in situ observations of NO_x and HO_x radicals, their precursors, and the radiation field were obtained in the lower stratosphere. We use these observations to evaluate the primary mechanisms that control NO_x-HNO_3 exchange and to understand their control over the partitioning between NO_2 and HNO_3 in regions of continuous sunlight. We calculate NO_x production (P_{NO_x}) and loss (L_{NO_x}) in a manner directly constrained by the in situ measurements and current rate constant recommendations, using approaches for representing albedo, overhead O_3 and [OH] that reduce model uncertainty. We find a consistent discrepancy of 18% between modeled rates of NO_x production and loss ($L_{NO_x} = 1.18P_{NO_x}$) which is within the measurement uncertainty of ±27%. The partitioning between NO_x production processes is [HNO_3 + OH (41 ± 2)%; $HNO_3 + h\nu$ (59 ± 2)%] and between NO_x loss processes is [NO_2 + OH, 90% to >97%; $BrONO_2 + H_2O$, 10% to <3%]. The steady-state description of NO_x-HNO_3 exchange reveals the significant influence of the tight correlation between the photolysis rate of HNO_3 and [OH] established by in situ measurements throughout the lower stratosphere. Parametrizing this relationship, we find (1) the steady-state value of $[NO_2]_{24h-avg}/[HNO_3]$ in the continuously sunlit, lower stratosphere is a function only of temperature and number density, and (2) the partitioning of NO_x production between HNO_3 + OH and $HNO_3 + h\nu$ is nearly constant throughout most of the lower stratosphere. We describe a methodology (functions of latitude, day, temperature, and pressure) for accurately predicting the steady-state value of $[NO_2]_{24h-avg}/[HNO_3]$ and the partitioning of NO_x production within these regions. The results establish a metric to compare observations of $[NO_2]_{24h-avg}/[HNO_3]$ within the continuously sunlit region and provide a simple diagnostic for evaluating the accuracy of models that attempt to describe the coupled NO_x-HO_x photochemistry in the lower stratosphere.

1. Introduction

The odd-nitrogen radicals ($NO_x \equiv NO + NO_2$) play an important role in the chemistry controlling the abundance of stratospheric ozone. NO_x radicals directly remove ozone through the catalytic cycling of NO and NO_2.[1,2] Through the coupling between the radical families, NO_2 and NO indirectly buffer the catalytic destruction of ozone by the halogen and hydrogen radicals, respectively.[3−7] The abundance of NO and NO_2 in the lower stratosphere is largely determined by the partitioning between NO_x and HNO_3, the dominant reservoir for odd-nitrogen ($NO_y \equiv HNO_3 + NO + NO_2 + NO_3 + 2N_2O_5 + HNO_4 + ClONO_2 + BrONO_2 + ...$). In situ and remote observations of the nitrogen species from ground stations, balloons, aircraft, and satellites have contributed to improving and evaluating our quantitative understanding of NO_x/HNO_3 (or NO_x/NO_y) using a variety of analytical approaches [e.g., refs 8−12 and references therein].

Figure 1 summarizes the predominant chemical reactions that determine the partitioning of NO_y in the lower stratosphere. The fast photochemistry that interconverts NO and NO_2 establishes a steady-state NO/NO_2 ratio on the time scale of seconds. The diurnal average partitioning between NO_2 and HNO_3 is estab-

◇ Part of the special issue "Harold Johnston Festschrift".

* Corresponding author. Address: 12 Oxford St., Harvard University, Cambridge, MA 02138. Tel: 617-495-5922. E-mail: kathy@huarp.harvard.edu.

† Harvard University.

‡ University of California, Berkeley.

§ Now at Department of Chemistry, University of Colorado, Boulder, CO 80309.

|| Now at Applied Materials, Santa Clara, CA 95054.

⊥ Divisions of Engineering and of Geological and Planetary Science, California Institute of Technology.

⊗ NOAA Aeronomy Laboratory.

▽ Now at Department of Chemistry and Biochemistry, Middlebury College, Middlebury, VT 05753.

NASA Jet Propulsion Laboratory, California Institute of Technology.

@ Meteorological Service of Canada.

¶ Now at Department of Marine Chemistry and Geochemistry, Woods Hole Oceanographic Institution, Woods Hole, MA 02543.

£ NASA Ames Research Center.

10.1021/jp002519n CCC: $20.00
Published on Web 01/05/2001

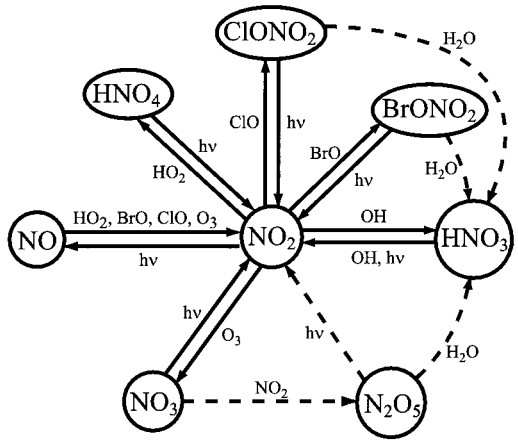

Figure 1. Schematic of primary species and reactions determining NO_y partitioning in the lower stratosphere. During extended periods of continuous sunlight, the chemistry controlling the partitioning between NO_2 and HNO_3 is greatly simplified with the minor reaction pathways (dashed lines) accounting for <8% of NO_2 to HNO_3 conversion.

TABLE 1: $NO_2 \leftrightarrow HNO_3$ Exchange Processes

$HNO_3 \rightarrow NO_2$ processes	
$HNO_3 + h\nu \rightarrow OH + NO_2$	(1)
$HNO_3 + OH \rightarrow NO_3 + H_2O$	(2a)
$NO_3 + h\nu \rightarrow NO_2 + O$ $NO_3 + h\nu \rightarrow NO + O_2$; $NO + O_3 \rightarrow NO_2 + O_2$	(2b)
$NO_2 \rightarrow HNO_3$ processes	
$NO_2 + OH \xrightarrow{M} HNO_3$	(3)
$NO_2 + NO_3 \xrightarrow{M} N_2O_5$	(4a)
$N_2O_5 + H_2O \xrightarrow{\text{aerosol}} 2HNO_3$	(4b)
$BrO + NO_2 \xrightarrow{M} BrONO_2$	(5a)
$BrONO_2 + H_2O \xrightarrow{\text{aerosol}} HOBr + HNO_3$	(5b)
$ClO + NO_2 \xrightarrow{M} ClONO_2$	(6a)
$ClONO_2 + H_2O \xrightarrow{\text{aerosol}} HOCl + HNO_3$	(6b)

lished by the slower reactions or series of reactions that exchange between NO_x and HNO_3. These exchange processes are summarized in Table 1. Throughout most of the lower stratosphere, the nighttime formation of N_2O_5 coupled with the heterogeneous hydrolysis of N_2O_5 on sulfate aerosols is an important pathway for conversion of NO_2 to HNO_3.[13−15] At high latitudes during summer, the presence of continuous sunlight inhibits the formation of N_2O_5, so that exchange between NO_x and HNO_3 is dominated by three gas-phase reactions:

$$HNO_3 + h\nu \rightarrow NO_2 + OH \quad \text{(R1)}$$

$$HNO_3 + OH \rightarrow NO_3 + H_2O \quad \text{(R2a)}$$

$$NO_2 + OH + M \rightarrow HNO_3 + M \quad \text{(R3)}$$

simplifying the photochemical description of the system. Under these conditions, we find that the hydrolysis of $BrONO_2$, N_2O_5, and $ClONO_2$ on sulfate aerosols typically accounts for less than 5%, 3%, and 0.002% of the conversion of NO_2 to HNO_3, respectively. Other potential sources of NO_x such as alkyl nitrates and PAN, which can be important in the troposphere and "lowermost" stratosphere, are not important at the altitudes being considered here, 15.2−20.5 km (potential temperatures of 418−542 K).[16]

Recently, a combination of observational and laboratory studies have led to significant improvements in model-measurement agreement under conditions where NO_x-HNO_3 exchange is dominated by gas-phase chemistry. Several studies using observations from the NASA ER-2 aircraft and balloon payloads obtained during the Photochemistry of Ozone Loss in the Arctic Region in Summer (POLARIS) mission found significant discrepancies in model-measurement comparisons of NO_x/NO_y when using reaction rate constants recommended by DeMore et al.[17] (JPL 1997).[12,18−21] Since the completion of the JPL 1997 compilation, new laboratory studies on the rate of $NO_2 + OH$[22,23] and $HNO_3 + OH$[24] have been published, showing substantial differences between the measured rates and recommended rates at stratospheric temperatures and pressures. At 230K and 55 mbar, the rate of $HNO_3 + OH$ recommended by Brown et al.[24] is 33% faster than JPL 1997. The rates of $NO_2 + OH$ recommended by Dransfield et al.[22] and Brown et al.[23] are 20% and 17% slower than JPL 1997, respectively. In a study of in situ observations from the ER-2, Gao et al.[18] found that while measured NO_x/NO_y exceeded modeled NO_x/NO_y by 35% using JPL 1997 recommendations, this value was lowered to 11% using the new rates; similar improvements were observed in the other studies. New recommendations for the rates of these two reactions are provided in the JPL 2000 supplement.[25]

Observations from the NASA ER-2 aircraft acquired during POLARIS provide a unique opportunity to examine the chemistry controlling the partitioning between NO_2 and HNO_3. During POLARIS, the instrument payload from previous ER-2 campaigns[26,27] was augmented to include in situ observations of NO_2 by direct laser-induced fluorescence (LIF)[28] and of $ClONO_2$ by resonance-fluorescence detection of ClO following the thermal decomposition of $ClONO_2$.[29] These new measurements improve our ability to assess the photochemistry of NO_x by (1) increasing confidence in our ability to accurately measure NO_2 as evidenced by the strong agreement between the measurements of NO_2 by LIF and those by the NOAA NO/NO_2/NO_y chemiluminescence instrument,[30] and (2) reducing uncertainty associated with inferences of $ClONO_2$.

In a recent analysis of NO_x-HNO_3 chemistry using ER-2 observations from POLARIS, Cohen et al.[12] used a chemical coordinate approach to evaluate the observations, concluding that the relative rate of HNO_3 formation through $NO_2 + OH$ and N_2O_5 hydrolysis is accurate when the new reaction rates are used. In addition, the study found that the fractional contribution of $HNO_3 + OH$ to total NO_x production (F_{HNO_3+OH}) spanned a very narrow range within the POLARIS data set and thus provided little information about the accuracy of our knowledge of the rate of $HNO_3 + OH$ relative to the photolysis of HNO_3. F_{HNO_3+OH} will vary with altitude; using the high-latitude, springtime measurements by the balloon-borne FIRS-2 instrument, Jucks et al.[19] found that F_{HNO_3+OH} dropped from ~0.4 to <0.1 at the highest altitudes of 35−40 km. The study examined the ratio of measured to modeled [HNO_3] as a function of the fractional contribution of HNO_3 photolysis to total production ($F_{HNO_3+h\nu}$) and found a tendency for measured/modeled HNO_3 to decrease from ~1 to ~0.8 as $F_{HNO_3+h\nu}$ increases from 0.6 to 0.9, indicating a possible error in the calculation of the HNO_3 photolysis rate.

Our analysis focuses on evaluating the primary mechanisms controlling NO_x-HNO_3 exchange in the continuously sunlit lower stratosphere and understanding their control over the partitioning between NO_2 and HNO_3 in this region. Thus, we effectively eliminate uncertainties associated with N_2O_5 formation and hydrolysis and examine the gas-phase chemistry in

isolation. Using in situ measurements of NO_2, NO, NO_y, OH, HO_2, ClO, O_3, $ClONO_2$, particle surface area, overhead O_3, temperature, and pressure, we develop an observationally constrained model of NO_x production and loss. This approach improves precision and accuracy in our analysis, helping to elucidate the factors controlling the behavior of the system in this region. Calculated production and loss, which should be equal in this model, are used to characterize (1) the overall accuracy of the model, (2) the precision with which the model captures atmospheric variation, and (3) the relative importance of the NO_x production and loss processes. By evaluating these observed characteristics in the context of a general steady-state description of NO_x-HNO_3 exchange, we show that the system is largely controlled by the relationship between the photolysis rate of HNO_3 (J_{HNO_3}) and the concentration of OH ([OH]). In situ measurements obtained throughout the lower stratosphere reveal a tight correlation between J_{HNO_3} and [OH]. We parametrize this relationship, developing a description of the NO_y partitioning which is fully consistent with the in situ observations. Using this parametrized chemistry, we create maps describing the average distribution of $[NO_2]_{24h-avg}/[HNO_3]$ in the region of continuous sunlight and the fractional contribution of $HNO_3 + OH$ to NO_x production throughout most of the lower stratosphere. These maps provide metrics useful for comparing observations across platforms, for evaluating the output of 2D and 3D chemical-transport models, and for exploring the variability in F_{HNO_3+OH} in the lower stratosphere.

2. Observations and Derived Quantities

During POLARIS, the ER-2 aircraft completed 25 flights between April and September 1997 with the majority of these flights originating from Fairbanks, Alaska (65° N, 150° W). In this paper, we restrict our analysis to observations obtained in regions of continuous sunlight and for which the NO_x-HNO_3 system is expected to be in diurnal steady state (DSS), i.e., no net exchange between NO_x and HNO_3 integrated over a day. In continuous sunlight, the DSS partitioning between NO_2 and HNO_3 is predominantly a function of temperature and pressure (section 4). In section 4, we show that this partitioning is independent of latitude provided the solar zenith angle (SZA) is less than approximately 75° at local noon and does not exceed 94°. Air parcels recently advected from latitudes outside of this region are not expected to be in DSS. Since the NO_x-HNO_3 system approaches DSS on a time scale roughly equal to the lifetime of NO_x ($\tau_{NO_x} \sim 3-8$ days with a median value of 5 days), we limit our analysis to observations that have satisfied these restrictions on SZA over the preceding lifetime of NO_x. In addition, the potential temperature (θ) at the time of measurement is required to be in excess of 400 K to eliminate measurements in the upper troposphere and "lowermost" stratosphere; this requirement effectively restricts the mixing ratio of O_3 to be greater than 0.8 ppm. We also require SZA < 80° at the time of measurement so that the concentration of OH is sufficiently large as to not introduce excessive uncertainty into the determination of [OH] throughout the day ([OH(time)] as described below). Approximately 2500 observations from five different flights satisfy these criteria. These observations range in altitude from 15.2 to 20.5 km (θ from 418 to 542 K) and temperature from 224 to 234 K. The flight date and latitude coverage of these observations are provided in Table 2.

NO_2 Observations. Two independent measures of NO_2 are available for the POLARIS mission. A new instrument designed for the in situ detection of NO_2, ClO, and $ClONO_2$ from the NASA ER-2 aircraft provided measurements of NO_2 using a direct laser-induced fluorescence (LIF) detection technique.[12,28] This instrument measured the concentration of NO_2 ($[NO_2]^{HRVD}$) with an estimated systematic uncertainty of ±10% ±50 pptv and an average precision of ±40 pptv for data reported at 10 s intervals, demonstrating that this technique is a sensitive and selective method for the in situ measurement of NO_2. (In the discussion of systematic errors, the notation ±*A*% ±*B* pptv is used where *A* indicates a multiplicative error and *B* indicates an additive error as would be representative of a zero offset.) The abundance of NO_2 was also measured using an NO chemiluminescence instrument designed to measure NO, NO_2, and NO_y; NO_2 was measured by first converting NO_2 to NO through photolysis and then detecting NO by chemiluminescence.[30,31] During the POLARIS mission, this instrument measured the concentration of NO_2 ($[NO_2]^{NOAA}$) with a systematic uncertainty of ±10−30% and an average precision of ±50 pptv for data reported at 1 s sample periods (±16 pptv when averaged to 10 s). In our analysis, we average the $[NO_2]^{NOAA}$ measurements to 10 s.

TABLE 2: Summary of Measurements

flight date	no. of observations	latitude range (°N)
970506	54	73.2−73.4
970513	303	72.4−82.5
970626	637	64.7−77.1
970704	304	65.2−71.1
970707	1206	66.2−89.8

The $[NO_2]^{HRVD}$ and $[NO_2]^{NOAA}$ measurements are in excellent agreement throughout the POLARIS mission, with a linear fit of the measurements giving $[NO_2]^{HRVD} \cong 1.07[NO_2]^{NOAA}$ and an $R^2 = 0.95$ where the intercept is fixed at zero.[30] No improvement in this fit is observed when the intercept is allowed to vary. For the purposes of this analysis, we combine the two sets of data by splitting the difference between the measurements and defining an average NO_2 concentration, $[NO_2] = (0.965 \times [NO_2]^{HRVD} + 1.035 \times [NO_2]^{NOAA})/2$ when both measurements are available, or $[NO_2] = 0.965 \times [NO_2]^{HRVD}$ or $[NO_2] = 1.035 \times [NO_2]^{NOAA}$ when only one is available. For both measures of NO_2, the systematic uncertainty is smallest at the highest altitudes where the mixing ratio of NO_2 is greatest. The typical systematic uncertainty for $[NO_2]^{HRVD}$ (including the ±50 pptv additive error) is ±13.5% at 20.3 km, ±16% at 18.3 km, and ±20% at 15.5 km [or at air number densities ([M]) of (1.7, 2.3, and 3.5) × 10^{18} molecules·cm^{-3}]. For $[NO_2]^{NOAA}$, the corresponding systematic uncertainties are ±11.5%, ±16%, and ±20%. Where both measures of NO_2 are available, the systematic uncertainty in the average $[NO_2]$ will be less than that due to either measurement alone. (Throughout this analysis, systematic uncertainties in the measurements and rates are assumed to be independent and random and are added in quadrature.) However, because both measures are not always available, we use the systematic uncertainty for $[NO_2]^{HRVD}$ as an upper limit to the uncertainty in this average $[NO_2]$.

Other In Situ Observations. In addition to the NO_2 observations, this analysis uses simultaneous observations of NO, NO_y, OH, HO_2, ClO, $ClONO_2$, O_3, H_2O, N_2O, pressure, temperature, and particle surface area density. The detection technique, reporting interval, systematic uncertainty (1σ), and precision (1σ) for these species are summarized in Table 3. We infer the measurement precision for the reporting interval by analyzing the scatter about a running median filter through the reported flight data. While these estimates are representative of the short-term precision of the instruments, they provide only a lower limit on the long-term precision of the measurements which will be influenced by systematic errors that vary flight-to-flight or over the duration of a flight. All observations are

TABLE 3: ER-2 In Situ Observations

species	detection technique	reference	reporting interval (s)	estimated systematic uncertainty (1σ)	average[a] precision (1σ)
NO_2^{HRVD}	laser-induced fluorescence	Perkins et al.[28]	10	±10% ±50 pptv	±40 pptv
NO_2^{NOAA}	photolysis/chemiluminescence	Del Negro et al.[30]	1	±10−30%	±50 pptv
NO	chemiluminescence	Fahey et al.[49]	1	±6% ±4 pptv	±13 pptv
NO_y	catalytic conversion/chemiluminescence	Fahey et al.[49]	1	±10% ±100 pptv	±80 pptv
OH	laser-induced fluorescence	Wennberg et al.[50]	2	±13% ±0.01 pptv	±0.03 pptv
HO_2	reaction with NO/ laser-induced fluorescence	Wennberg et al.[50]	2	±15% ±0.01 pptv	±0.15 pptv
H_2O	photofragment fluorescence	Hintsa et al.[51]	4	±5%	±0.11 ppmv
ClO	resonance fluorescence	Bonne et al.[29]	35	±15%	±3 pptv
$ClONO_2$	thermal dissociation/ resonance fluorescence	Bonne et al.[29]	35	±20%	±10 pptv
O_3	UV absorption	Proffitt et al.[52]	1	±5%	±6 ppbv
N_2O^{ATLAS}	laser absorption spectroscopy	Podolske and Loewenstein[53]	1	±2.5%	±1.8 ppbv
N_2O^{ALIAS}	laser absorption spectroscopy	Webster et al.[54]	3	±5%	±1.3 ppbv
O_3 column over ER-2	spectroradiometer	McElroy[42]	132	±3%	±1 DU
pressure	pressure sensor	Scott et al.[55]	1	±0.3 mbar	±0.06 mbar
surface area	aerosol spectrometer	Jonsson et al.[56]	30	±60%	±0.03 $\mu m^2/cm^3$
temp	temp sensor	Scott et al.[55]	1	±0.3 K	±0.25 K

[a] Average precision at the reporting interval.

averaged to 10 s prior to analysis. For the species reported less frequently ([ClO], $[ClONO_2]$, and particle surface area density), linear interpolation is used to infer the concentration between measurements. The ClO and $ClONO_2$ data are smoothed using a running median filter with a time interval of 3 and 1.5 min, respectively, prior to interpolation.

Photolysis Rates. The photolysis rate for a chemical species depends on the absorption cross section of the species, the quantum yield for dissociation, and the actinic flux. For this paper, local radiative conditions are determined using a radiative transfer model described by Prather et al.[32] and used in the analysis of stratospheric observations.[11,20,33] The radiative transfer model accounts for the principle factors influencing the radiative conditions—SZA, ozone column above the ER-2 (overhead O_3), albedo, cloud height, and local temperature. Absorption cross sections and quantum yields are based on the JPL 1997 recommendations.[17] For the production of $O(^1D)$ from the photolysis of O_3, the quantum yields recommended by Michelsen et al.[34] are used. The JPL 2000 supplement provides a new recommendation for the quantum yield of $O(^1D)$; for the calculation of HO_x production discussed in the next section, the impact of this new recommendation is small (<5%). Photolysis rates are calculated at 1−5 min intervals along the ER-2 flight track and linear interpolation is used to infer photolysis rates between these points. At each of these points, the diurnal behavior of the photolysis rates is characterized by running the radiative-transfer model from midnight to midnight at 15 min intervals.

HNO_3. The concentration of HNO_3 is calculated from measurements of NO_y, NO_2, NO, and $ClONO_2$ as

$$[HNO_3] = [NO_y] - [NO_2] - [NO] - [ClONO_2] - [HNO_4]_{SS} \quad (1)$$

where $[HNO_4]_{SS}$ is the calculated steady-state concentration and $[BrONO_2]$ is negligible. For the data included in this analysis, the typical partitioning of NO_y is 14% NO_2, 10% NO, 3% $ClONO_2$, and 3% HNO_4. The remaining 70% is assumed to be HNO_3. Since the formation of N_2O_5 is inhibited by continuous solar illumination, these air parcels tend to have <0.3% of NO_y present as N_2O_5. Using a systematic uncertainty of ±16% for NO_2 and those given in Table 3 for NO_y, NO, and $ClONO_2$, estimating a possible error of $\times 1.3/\div 3$ for HNO_4, and assuming the errors are independent, the systematic uncertainty in $[HNO_3]$ is calculated to be ±17% (including the ±100 pptv additive error in NO_y) for the typical mixing ratio of HNO_3.

Diurnal Variation in NO_2, OH, and $BrONO_2$. Under conditions of continuous sunlight, the diurnal variations in $[NO_x]$ and $[HNO_3]$ are negligible, approximately 3% and 1%, respectively. With $[NO_x]$ constant, the diurnal behavior of $[NO_2]$ is controlled by the diurnal variation in the partitioning between NO and NO_2. This partitioning is established by the dominant exchange processes—the photolysis of NO_2 and the reactions of NO with O_3 and ClO. The contribution from the other NO−NO_2 exchange processes—the reactions of NO with BrO and HO_2—is negligible (<2%). Thus, the SZA dependence of NO/NO_2 is determined by the SZA dependence of J_{NO_2} and ClO and is well described by the instantaneous steady-state relationship; for POLARIS, Del Negro et al.[30] report an average discrepancy of 6% between observations of NO/NO_2 and the steady-state relation. Specifically, the diurnal variation in $[NO_2]$ is given by

$$[NO_2(\text{time})] = \frac{[NO_x]}{\left(\frac{[NO]}{[NO_2]} + 1\right)} = \frac{[NO_x]}{\left(\frac{J_{NO_2}(\text{time})}{k_{NO+O_3}[O_3] + k_{NO+ClO}[ClO(\text{time})]} + 1\right)} \quad (2)$$

where $[NO_x]$ and $[O_3]$ are measured directly and a parametrization of ClO with SZA, constrained to match the measurement, is used to describe the diurnal behavior of ClO.

This method of determining the concentration of NO_2 over a 24 h period is based only on in situ observations and the well-understood NO/NO_2 ratio; thus, the systematic uncertainty in $[NO_2(\text{time})]$ is close to that of the measurements themselves. The systematic uncertainty of $[NO_2(\text{time})]$ is estimated to be ±13%, ±14%, and ±16% for [M] equal to (1.7, 2.3, and 3.5) $\times 10^{18}$ molecules·cm^{-3} given the corresponding uncertainty in the concentration of NO_x—±8%, ±10%, and ±12% at these values of [M]—and that estimated for the quantity ($[NO]/[NO_2] + 1$), ±10%. The percentage uncertainty in NO_x is less than that of NO_2 because of the accuracy of the NO measurements.

The concentration of OH is important to the calculation of NO_x production and loss rates. Despite the complexity of HO_x photochemistry, the concentration of OH in the lower stratosphere is observed to be tightly correlated with solar zenith angle.[35,36] The SZA dependence of [OH] observed during POLARIS is used to describe [OH] as

$$[\mathrm{OH(time)}] = [\mathrm{OH}]_0(94 - \mathrm{SZA(time)})/(94 - \mathrm{SZA}_0) \quad (3)$$

where $[OH]_0$ and SZA_0 are the values at the time of measurement.

The concentration of $BrONO_2$ over the 24 h integration period is calculated from estimates of total inorganic bromine (Br_y) and the instantaneous steady-state partitioning of the major inorganic bromine species (BrO, $BrONO_2$, HOBr, and HBr) constrained by in situ measurements where possible. The value of Br_y is estimated using measurements of N_2O together with an N_2O-Br_y relationship.[37] For the data considered here, the calculated concentration of $BrONO_2$ and the concentration found using the full photochemical steady-state model of Salawitch et al.[33] agree well, with an average difference of only $1 \pm 4\%$. The estimated systematic uncertainty in $[BrONO_2]$ is $\pm 35\%$ and is dominated by the uncertainty in Br_y.

For this analysis, calculations are performed using JPL 1997 recommendations[17] with updates provided in the JPL 2000 supplement[25] for all rate constants and reaction probabilities.

3. Evaluating the Model of NO_x-HNO_3 Exchange Processes

In this section, we present a detailed analysis of our understanding of the processes that control NO_x-HNO_3 exchange in regions of continuous sunlight, providing a framework in which to examine the behavior of the system from the more general approach taken in section 4. We use calculations of the production and loss of NO_x integrated over the day, P_{NO_x} and L_{NO_x}, to quantify (1) the accuracy of our model of NO_x-HNO_3 exchange through the agreement between P_{NO_x} and L_{NO_x}, (2) the precision of our model (e.g., its ability to capture atmospheric variation) through the scatter in P_{NO_x}/L_{NO_x}, and (3) the relative importance of the various NO_x production and loss mechanisms.

Through the strict selection criteria, we specifically isolate the system of gas-phase NO_x-HNO_3 exchange processes and limit the analysis to observations for which we expect the NO_x-HNO_3 system to be in diurnal steady state. For these conditions, only the reactions R_{HNO_3+OH}, $R_{HNO_3+h\nu}$, R_{NO_2+OH}, and $R_{BrONO_2+H_2O}$ are important. (Throughout this paper, we will use the abbreviation R_{X+Y} to refer to the reaction of species X with Y. Similarly, the rate constant for the reaction of species X with Y and the photolysis rate of species X will be written as k_{X+Y} and J_X, respectively.) P_{NO_x} and L_{NO_x} are calculated directly from the in situ observations and the expected diurnal behavior of the participating species (section 2):

$$P_{NO_x} = \int_{24h} J_{HNO_3}[HNO_3]\,dt + \int_{24h} k_{HNO_3+OH}[OH][HNO_3]\,dt \quad (4)$$

$$L_{NO_x} = \int_{24h} k_{NO_2+OH}[OH][NO_2]\,dt + \int_{24h} k_{BrONO_2+H_2O}[BrONO_2]\,dt \quad (5)$$

Because we select for parcels in DSS, we expect $P_{NO_x} = L_{NO_x}$ and $P_{NO_x}/L_{NO_x} = 1$. The discrepancy between the computed values of P_{NO_x}/L_{NO_x} and the expected value of 1 is a measure of the error in our calculation. This discrepancy may arise from errors in the observations, the calculated photolysis rates, or the rate constants, as well as through omissions in the chemical description of the system. We note that any small deviations from DSS would tend to be random, increasing the scatter in P_{NO_x}/L_{NO_x} but not introducing a bias.

Factors that degrade the accuracy and precision of our analysis can significantly influence our interpretation of the NO_x system or mask characteristics that provide insight into the behavior of NO_2-HNO_3 partitioning. Poor precision creates scatter in the data, but does not affect the average value of P_{NO_x}/L_{NO_x} (because of the large number of observations). Any systematic error, however, will shift P_{NO_x}/L_{NO_x} from the expected value of 1. We first focus on identifying and minimizing the effect of these factors. Specifically, we show that albedo, overhead O_3, and OH exert sufficient control over the NO_x-HNO_3 system that inaccuracy or imprecision in these terms can introduce enough uncertainty or scatter to hamper our analysis.

Factors Influencing Precision and Accuracy of NO_x-HNO_3 Models. *A. Albedo*. The calculated photolysis rate of NO_2 is sensitive to albedo.[38] Often, the albedo below the air parcel at the time of measurement, the "instantaneous albedo", is used to assess NO_x chemistry. While the observed partitioning of NO_x between NO and NO_2 will reflect this albedo, the observed partitioning between NO_x and HNO_3 reflects average NO_2 to NO partitioning conditions, rather than instantaneous conditions. Thus, NO_x/HNO_3 depends on the albedo history of the air parcel over a period of days (on the order of 3−8 days). We capture this history by integrating daily TOMS reflectivity data with 10 day back trajectories calculated using the Goddard Space Flight Center (GSFC) Isentropic Trajectory Model. These trajectories are available for air parcels at 7 min intervals along the ER-2 flight track.

We define an "effective albedo" for the NO_x-HNO_3 system as a weighted average of the albedo along the back trajectory. Assuming that the diurnal steady-state ratio of NO_x to HNO_3 is established on a time scale equivalent to the lifetime of NO_x and that this ratio will reflect the albedo over the most recent history more strongly than the albedo experienced days prior to observation, we define the effective albedo as

$$A_{\mathrm{effective}} = \frac{\int_0^{-\tau_{NO_x}} A(t)\exp(t/\tau_{NO_x})\,dt}{\int_0^{-\tau_{NO_x}} \exp(t/\tau_{NO_x})\,dt} \quad (6)$$

where $A(t)$ is the albedo along the back trajectory. An unweighted average of the albedo along the back trajectory is typically within ± 0.05 of this method; the instantaneous albedo differs from the effective albedo by up to 0.6. Linear interpolation is used to estimate the effective albedo between back-trajectory calculations. For photolysis rates calculated using effective albedo, an average cloud height of 590 mbar is used.

In the calculation of P_{NO_x} and L_{NO_x}, we determine $[NO_2]$ from the direct measurement of NO_x and the steady-state relation for NO/NO_2 (eq 2), using the effective albedo to calculate J_{NO_2}. This describes the partitioning between NO and NO_2 over the time period in which the exchange between NO_x and HNO_3 established a steady state. The result of using the effective albedo is seen in Figure 2 where we plot the percent deviation from the mean P_{NO_x}/L_{NO_x} versus the difference between the effective and instantaneous albedo. In panel a, the instantaneous albedo is used to determine the partitioning between NO and NO_2. When the instantaneous albedo is much less than the effective albedo, the calculated $[NO_2]$ will be higher than actually

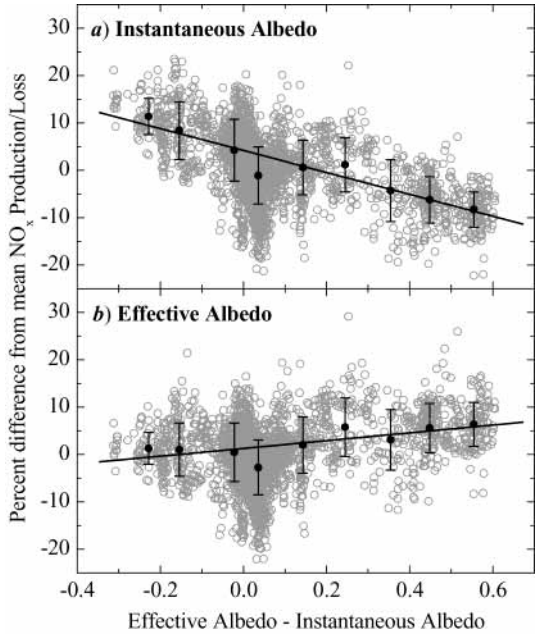

Figure 2. Percent difference from mean value of P_{NO_x}/L_{NO_x} versus the difference between effective and instantaneous albedo, where the instantaneous albedo (panel a) or effective albedo (panel b) has been used to infer NO_x loss rates. For each set of calculations, the average value and standard deviation of the measurements are calculated for equally spaced intervals along the abscissa.

experienced over the preceding few days and NO_x loss through $NO_2 + OH$ will be overestimated, resulting in an artificially low value for P_{NO_x}/L_{NO_x}. Similarly, when the instantaneous albedo is much greater than the effective albedo, $[NO_2]$ will be lower than average, NO_x loss will be underestimated, and P_{NO_x}/L_{NO_x} will be artificially high. This trend is observed in the data. The use of effective albedo reduces the dependence of P_{NO_x}/L_{NO_x} on the difference between effective and instantaneous albedo by a factor of 3.

While some of the other factors influencing the partitioning between NO and NO_2, namely O_3, temperature, ClO, BrO, and HO_2, vary significantly within the data set due to the range in altitude, location, and time of the observations, the changes along the back trajectory of the air parcel are relatively small and we use the conditions at the flight intercept in assessing the partitioning between NO and NO_2. The difference between the temperature at the time of measurement and the weighted average along the back trajectory is <2 K for 90% of the data (3.6 K max), corresponding to a difference of $<2\%$ in NO_2 for these points (4.4% max). The use of a weighted-average temperature in eq 2 would account for this effect, but does not alter the conclusions of this analysis. O_3 is expected to be largely invariant over the period of a few days; Fahey et al.[39] report a maximum net ozone loss rate of 15%/month. Finally, ClO, BrO, and HO_2 are sufficiently minor contributors that even relatively large changes are insignificant.

Figure 2 demonstrates that the use of instantaneous albedo in assessing NO_x-HNO_3 partitioning may either introduce additional scatter or a bias into an analysis (e.g., in cases where all of the data are collected over an ice sheet, the instantaneous albedo will be systematically larger than the effective albedo). Using the effective albedo reduces this source of error and is more appropriate for assessing NO_x-HNO_3 partitioning. These results are in agreement with a recent study by Voss et al.[40] in which use of a climatological average albedo reduces scatter in model-measurement comparisons of $ClONO_2$/HCl where the time constant for the system is 5 to 10 days.

TABLE 4: HO_x Production and Loss Processes[a]

HO_x production			HO_x loss		
reaction	yield	% of P_{HO_x}	reaction	yield	% of L_{HO_x}
$H_2O + O(^1D)$	2	34 ± 4	$HNO_3 + OH$	1	15 ± 1
$CH_4 + O(^1D)$	2	6.1 ± 0.9	$HNO_4 + OH$	1	12 ± 1
$H_2 + O(^1D)$	2	1.7 ± 0.2	$NO_2 + OH$	1	40 ± 3
$HNO_3 + h\nu$	1	30 ± 3	$HCl + OH$	1	5.8 ± 0.6
$HNO_4 + h\nu$	1	12 ± 2	$HO_2 + OH$	2	5.7 ± 1.6
$H_2CO + h\nu$[b]	2	12 ± 2	$HO_2 + NO_2$	1	21 ± 3
$CH_4 + Cl$	1	5.0 ± 2.4			

[a] Percentages reported for calculations using JPL 2000 and J^{INSITU}. [b] Only the $H_2CO + h\nu \rightarrow H + HCO$ channel is counted as a HO_x source.

B. Overhead O_3. Because HNO_3 photolyzes primarily in the UV, uncertainty in the calculation of NO_x production is introduced through uncertainty in overhead O_3. Studies of NO_x chemistry using aircraft measurements use a variety of techniques to determine overhead O_3. In this section, we evaluate two common techniques, isolating and quantifying the uncertainty in P_{NO_x} associated with imprecision in overhead O_3. This analysis provides a measure of the uncertainty introduced by overhead O_3 in prior analyses using these techniques and highlights the importance of a precise measure of overhead O_3 for analyses relying on high precision to isolate errors in NO_x (or HO_x) photochemistry (e.g., ref 12). We consider the following methods of determining overhead O_3:

(1) Satellite measurements of the total ozone column may be combined with a vertical distribution of O_3 to infer overhead O_3. For POLARIS, a latitude-dependent climatology for the vertical distribution of O_3 for each POLARIS deployment is developed based on local profiles provided by ozonesondes deployed from Fairbanks, AK, in situ O_3 measurements obtained during ascent, descent, and vertical dives of the ER-2, and a satellite-based climatology for profiles of O_3[41] that is used for altitudes above those accessible by ozonesondes. These climatological O_3 profiles are multiplied by a constant factor to scale them to match measurements of total ozone column by the Earth Probe TOMS instrument. The estimated total uncertainty in these overhead O_3 calculations is ± 20 DU, and photolysis rates calculated using overhead O_3 inferred in this manner are denoted $J^{SATELLITE}_{SPECIES}$.

(2) Spectrally resolved measurements of the radiation field from an on-board radiometer may be used to infer overhead O_3. During POLARIS, the Composition and Photodissociative Flux Measurement (CPFM) instrument[42] on board the ER-2 measured the radiation field from 300 to 800 nm, providing a simultaneous measure of overhead O_3 with an estimated systematic uncertainty of $\pm 3\%$ and a precision of ± 1 DU. CPFM estimates of overhead O_3 for large solar zenith angles, i.e., SZA $> 80°$, are not used due to a significant decline in the precision and accuracy of the measurement. Photolysis rates calculated using CPFM estimates of overhead O_3 are denoted $J^{INSITU}_{SPECIES}$.

To evaluate these measures of overhead O_3, we combine the analysis of the NO_x system described above with an analogous, but distinct, analysis of the HO_x ($OH + HO_2$) system that is constrained by in situ measurements. Hanisco et al.[36] examine the chemistry controlling the production and loss of HO_x in the lower stratosphere. In Table 4, we summarize the relative importance of the primary reactions controlling HO_x production and loss in the high-latitude, lower stratosphere during summer. Under these conditions, HO_x is in instantaneous steady-state. We use the model of HO_x chemistry described by Hanisco et al.[36] together with the in situ measurements, photolysis rates

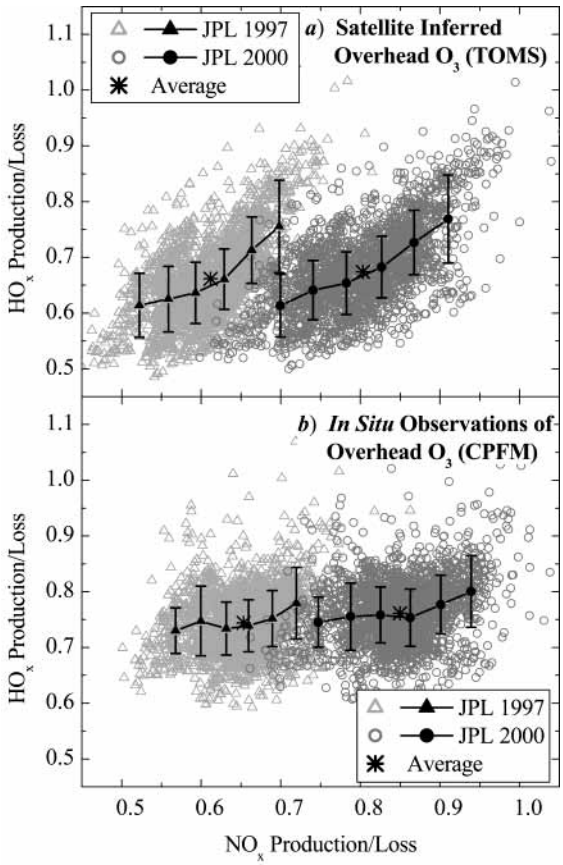

Figure 3. P_{HO_x}/L_{HO_x} versus P_{NO_x}/L_{NO_x} inferred from in situ measurements in regions of continuous sunlight. The production and loss rates are determined for both JPL 1997 (△, ▲) and JPL 2000 (○, ●) rate constants. Satellite-inferred (TOMS) and in situ based (CPFM) overhead O_3 estimates are used to calculate photolysis rates for the results in panels a and b, respectively. For each set of calculations, the average value and standard deviation of the measurements are calculated for equally spaced intervals along the abscissa as well as the overall average (∗).

calculated using instantaneous albedo, and the recommended reaction rate constants to directly calculate the instantaneous production and loss rates for HO_x (P_{HO_x} and L_{HO_x}). P_{HO_x} and L_{HO_x} are only calculated for measurements at SZA < 70° where HO_x modeling is more accurate.[36] As with the NO_x analysis, systematic errors in any of the inputs will shift P_{HO_x}/L_{HO_x} away from the expected value of 1, while imprecision in an input will introduce scatter into P_{HO_x}/L_{HO_x}.

In the lower stratosphere, the photochemistry of the HO_x and NO_x systems are highly coupled, e.g., through the reactions R_{NO_2+OH}, R_{HNO_3+OH}, and $R_{HNO_3+h\nu}$. These calculations of P_{HO_x}/L_{HO_x} and P_{NO_x}/L_{NO_x} are constrained by the same reaction rates, photolysis rates, and in situ measurements. The advantage of this analysis is that these calculations are independent so that errors in the HO_x photochemical model are not propagated to our assessment of NO_x and vice versa. The analyses will both reflect imprecision or errors in common terms.

In Figure 3, P_{HO_x}/L_{HO_x} is plotted against P_{NO_x}/L_{NO_x} using either satellite-based (panel a) or in situ-based (panel b) estimates of overhead O_3 to calculate photolysis rates. In panel a, the results using the satellite-based overhead O_3 estimates show a positive correlation between P_{NO_x}/L_{NO_x} and P_{HO_x}/L_{HO_x}. The ratios calculated using in situ based estimates of overhead O_3 shown in panel b are more compact in both P_{NO_x}/L_{NO_x} and P_{HO_x}/L_{HO_x} and exhibit no significant correlation. A correlation between these ratios occurs when there is imprecision in a term with significant influence over both systems. Both the HO_x and NO_x systems are sensitive to overhead O_3. While the large number of production and loss terms in the HO_x system reduces the sensitivity of P_{HO_x} and L_{HO_x} to errors in any single rate constant or photolysis rate, all HO_x production processes are directly dependent upon UV flux and thus upon the estimate of overhead O_3 used in calculating the photolysis rates. In addition, NO_x production has a strong dependence on UV flux through the photolysis of HNO_3. Intra- or interflight precision of roughly ±15 DU overhead O_3 would be necessary to account for the extent of the correlation. The determination of overhead O_3 from satellite observations (TOMS) is based on limited information on the ozone profile. Because the difference between the actual and assumed ozone profile can vary over the spatial range of an ER-2 flight or from flight to flight, the direction and magnitude of the systematic bias in the overhead O_3 estimates using this method are variable, probably degrading the long-term precision to that of the systematic uncertainty (±20 DU) and accounting for the correlation observed in panel a. Because the correlation of errors is absent when in situ based estimates of overhead O_3 provided by CPFM are used, this analysis demonstrates that in situ based estimates of overhead O_3 are significantly more precise than that based on satellite measurements of the total O_3 column and climatological O_3 profiles. While the CPFM instrument has participated in ER-2 missions since 1993, the CPFM measure of overhead O_3 has not been extensively used in analyses of ER-2 observations, at least in part because the value of its more precise representation of overhead O_3 was under appreciated. In this analysis, we use $J^{INSITU}_{SPECIES}$ where available, reducing the standard deviation expressed as a percent of the mean (a measure of the scatter) from 11.1% to 7.5% for P_{HO_x}/L_{HO_x} and 8.2% to 6.5% for P_{NO_x}/L_{NO_x}.

We note that variations in overhead O_3 along the back trajectory should not significantly affect the NO_x-HNO_3 system under conditions of continuous sunlight. While both the photolysis rate of HNO_3 and the concentration of OH are important in NO_x-HNO_3 exchange and both quantities are affected by overhead O_3, we show in section 4 that it is the ratio $\int_{24h} J_{HNO_3}/\int_{24h}[OH]$ that drives the NO_2-HNO_3 partitioning and that this ratio is nearly constant in regions of continuous sunlight.

C. OH. Throughout the lower stratosphere, OH exerts significant control over the partitioning between NO_2 and HNO_3 such that differences in the treatment of OH can affect the interpretation of analyses of NO_x chemistry. In our analysis of the HO_x system, we use the in situ measurements to directly constrain the calculation of P_{HO_x} and L_{HO_x} which allows assessment of the accuracy of HO_x photochemistry. The average value of P_{HO_x}/L_{HO_x} calculated using the reaction rate constants recommended by JPL 2000 and the in situ based estimates of overhead O_3 is 0.76 ± 0.06 compared to the expected value of 1. We note that while the use of JPL 2000 instead of JPL 1997 significantly shifts P_{NO_x}/L_{NO_x} toward the expected value of 1, no improvement is observed in the ratio P_{HO_x}/L_{HO_x} (P_{HO_x}/L_{HO_x} = 0.74 ± 0.05 for JPL 1997). In the HO_x system, the updates in JPL 2000, an increase in k_{HNO_3+OH} and a decrease in k_{NO_2+OH}, tend to cancel because both reactions are HO_x loss processes. The value of P_{HO_x}/L_{HO_x} is near the limit of the estimated 1σ uncertainty associated with the in situ measurements alone (±30%).

Using this same model, calculations of [OH] constrained by the in situ measurements would underestimate [OH] by 30% when compared to the measured [OH] ($[OH]_{meas} = 1.3[OH]_{calc}$). This level of discrepancy between measured and modeled

[OH] can influence our interpretation of the accuracy of NO_x chemistry. For instance, using $[OH]_{calc}$ in our analysis of P_{NO_x}/L_{NO_x} would lead to a value of about 1.0, compared to the value of 0.85 that is found using measured [OH]. In a recent analysis of the POLARIS data using a trajectory model to examine the radical species, Pierson et al.[21] found modeled [OH] to be 22% lower than measured when using JPL 1997 rates and 30% lower than measured when using the new rates recommended by Brown et al.[23,24] The authors attribute the change in the model-measurement agreement of [OH] to the chemical coupling between HO_x and NO_x within the trajectory model. The discrepancy between calculations of [OH] and measured [OH] varies significantly within the observational data set of the ER-2; in the 1994 ASHOE/MAESA mission with the bulk of observations in the mid-to-high latitudes of the southern hemisphere from fall through spring, $[OH]_{calc} = (1.1 \pm 0.2)[OH]_{meas}$.[36] In our analysis of NO_x chemisty, we eliminate the influence of errors in HO_x chemistry and the influence of the feedback between HO_x and NO_x by using the in situ measurements of OH which are reported to be accurate to ±13% (Table 3).

Assessing the NO_x−HNO_3 Photochemical Model. The values of P_{NO_x}/L_{NO_x} calculated using the recently revised JPL 2000 rate constants are plotted versus [M] in Figure 4a. The average value of P_{NO_x}/L_{NO_x} is 0.85 ± 0.06, compared to an expected value of 1. Equivalently, $L_{NO_x} = 1.18P_{NO_x}$. The combined uncertainties in [NO_2(time)] (±13% to ±16%), [OH-(time)] (±13%), and HNO_3 (±17%) result in a systematic uncertainty for P_{NO_x}/L_{NO_x} of about ±27% over the range of [M] presented. On the basis of current JPL recommendations, the uncertainties in k_{NO_2+OH} and J_{HNO_3} at 230 K are estimated to be times/divide 1.15 and 1.3, respectively. JPL 2000 reports an uncertainty factor of 1.15 for k_{HNO_3+OH} at 298 K;[25] we use a factor of 1.3 to account for the added uncertainty at 230 K. These uncertainties increase the total systematic uncertainty in P_{NO_x}/L_{NO_x} to +37%/−34%. Using a linear least-squares fit to the data, we find that P_{NO_x}/L_{NO_x} exhibits almost no trend with [M]; the observed change in P_{NO_x}/L_{NO_x} for a 10^{18} molecules·cm^{-3} change in [M] is −1.3%. Thus, both the primary exchange reactions between NO_x and HNO_3 and their combined [M] dependence using the JPL 2000 recommendations are consistent with the observations under conditions dominated by gas-phase processes.

In Figure 4, panels b and c, we present the fractional contribution of the four principal reactions, R_{HNO_3+OH}, $R_{HNO_3+h\nu}$, R_{NO_2+OH} and $R_{BrONO_2+H_2O}$, to the production and loss of NO_x. This measure of the partitioning between the NO_x production and loss processes in this region is directly constrained by in situ measurements of the principle species involved, i.e., NO_2, OH, and NO_y. Partitioning between the two production reactions is remarkably constant in the summertime high latitudes with HNO_3 photolysis accounting for (59 ± 2)% and HNO_3 + OH accounting for (41 ± 2)% of the production. This consistency persists despite the significant variability in the terms influencing the photolysis rate of HNO_3 and the concentration of OH that results from sampling over a large spatial (latitudinal and vertical) and seasonal extent. These air parcels experienced a range of solar exposure conditions from cases where the SZA remained almost constant near 67° to cases where the SZA varied between 41° and 92° over the course of the day. In addition, the overhead O_3 in this data set varies by a factor of 2, ranging from 150 to 300 DU, with a corresponding change in J_{HNO_3} (normalized to a SZA of 67.5°) of $(2.9-5.0) \times 10^{-7}$ s^{-1}. Finally, many other factors involved in the production and loss of OH show considerable variation, including among others HNO_3 [$(5.9-16.8) \times 10^9$ molecules·cm^{-3}], O_3 [$(2.9-6.4) \times 10^{12}$ molecules·cm^{-3}], H_2O [$(7.6-15.7) \times 10^{12}$ molecules·cm^{-3}], and NO_2 [$(5.7-32.5) \times 10^8$ molecules·cm^{-3}]. The partitioning between the NO_x production processes remains constant despite this variability due to a strong correlation between J_{HNO_3} and [OH] combined with the narrow range of observed temperatures (224−234 K). This correlation is central to generalizing the behavior of the NO_x−HNO_3 system which is discussed in section 4. In a detailed analysis of HO_x chemistry, Hanisco et al.[36] present the processes which combine to make [OH] in the lower stratosphere primarily a function of SZA and overhead O_3.

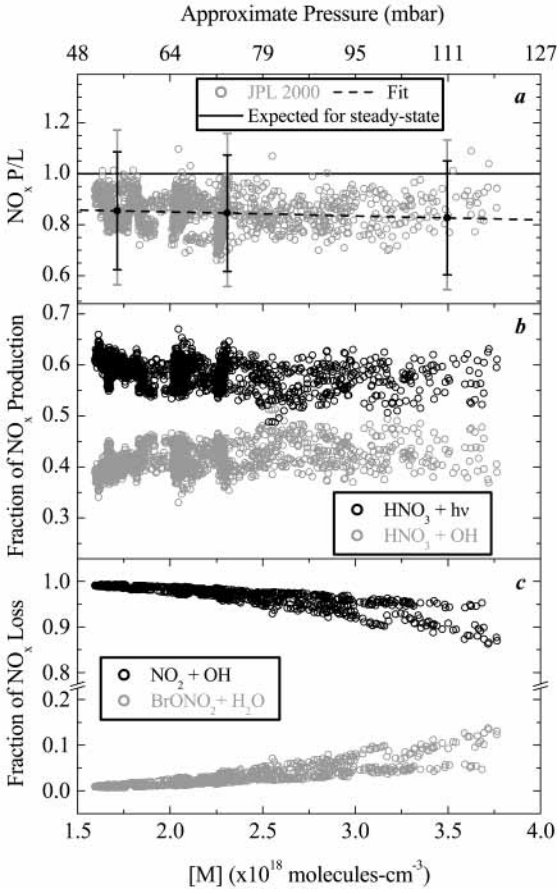

Figure 4. (a) P_{NO_x}/L_{NO_x} versus [M] inferred from in situ measurements obtained in continuous sunlight and JPL 2000 rate constants. The black dashed line is a linear least-squares fit to the data and the solid line marks the expected value of 1. The black error bars represent the total estimated systematic uncertainty from uncertainties in OH, HNO_3, and NO_2. The gray error bars indicate additional uncertainty associated with uncertainties in the rate constants and photolysis rates. (b) Fractional contribution of HNO_3 photolysis (O) and reaction with OH (light gray circles) to total NO_x production for the measurements included in panel a. (c) Fractional contribution of the reaction NO_2 + OH (O) and the hydrolysis of $BrONO_2$ (light gray circles) to total NO_x loss for the measurements included in panel a.

During periods of continuous sunlight, the NO_x loss rate is dominated by the recombination of OH and NO_2 to form HNO_3. The fraction of NO_x loss through $BrONO_2$ hydrolysis is small, decreasing from 5 to 10% at [M] = 3.5×10^{18} molecules·cm^{-3} to less than 3% at [M] < 2×10^{18} molecules·cm^{-3}. This trend is primarily related to a decrease in aerosol surface area density with increasing altitude. Surface area density decreases from about 2 to 0.5 μm^2/cm^3 over the range of altitudes represented in Figure 4c. The fractional contribution of $BrONO_2$ hydrolysis

to the total loss rate separates into two distinct populations at $[M] > 3 \times 10^{18}$ molecules·cm^{-3}. This separation is related to SZA exposure throughout the day and is present, although not obvious, throughout the data set. Because $BrONO_2$ hydrolysis proceeds throughout the day while the reaction of NO_2 with OH slows significantly as [OH] decreases at larger SZA, observations for which SZA at local midnight exceeds 87° tend to exhibit a larger fractional contribution from $BrONO_2$ hydrolysis than those for which SZA is less than 87° throughout the day.

The use of effective albedo and in situ based overhead O_3 contributes to the precision of the results in Figure 4. The use of measured OH contributes to their accuracy; since approximately 40% of NO_x production proceeds through $HNO_3 + OH$ and $[OH]_{calc} \sim 0.77[OH]_{meas}$, the use of calculated OH would result in a ~15% higher value for average P_{NO_x}/L_{NO_x} with a much greater uncertainty. Uncertainty in calculated OH can obscure errors in the NO_x chemistry; the difference between measured and calculated [OH] is of the same order as the recent changes to the rate constants, k_{NO_2+OH} and k_{HNO_3+OH}.

Overall, the new JPL 2000 rate constant recommendations significantly improve the photochemical description of NO_x-HNO_3 exchange; the JPL 1997 rates result in an average P_{NO_x}/L_{NO_x} of 0.65 ± 0.05 and introduce an [M] dependence of (−7%)/(10^{18} molecules·cm^{-3}). While the improvement in the average value of P_{NO_x}/L_{NO_x} is attributable to changes in k_{NO_2+OH} and k_{HNO_3+OH}, the reduction in the observed [M] dependence is due to the change in the recommended reaction probability for the heterogeneous hydrolysis of $BrONO_2$ ($\gamma_{BrONO_2+H_2O}$). Consistent with the laboratory studies of Hanson et al.,[43] JPL 2000 models $\gamma_{BrONO_2+H_2O}$ as a function of H_2SO_4 wt % (ω) where $\gamma_{BrONO_2+H_2O}$ equals about 0.8 at $\omega < 70\%$, but decreases sharply at higher ω. For the present data set, ω ranges from 74.6% to 80.2% with a corresponding range in $\gamma_{BrONO_2+H_2O}$ of 0.41 to 0.16, significantly less than the value of 0.8 recommended by JPL 1997. Since the fractional contribution of $BrONO_2$ hydrolysis increases with [M] (Figure 4c), an overestimate of this term will produce an [M] dependence in the ratio P_{NO_x}/L_{NO_x}.

While we cannot rule out measurement error as the source of the remaining discrepancy between calculated P_{NO_x} and L_{NO_x}, the discrepancy could result from errors in the rate constants, the photolysis rates, or the description of the system, requiring either a 30% increase in k_{HNO_3+OH}, a 45% increase in the photolysis of HNO_3, a 15% reduction in k_{NO_2+OH}, or some combination for the photochemical description to be in exact agreement with the measurements. There is some evidence that k_{NO_2+OH} may be lower than the JPL 2000 value used here. First, the functional fit to the laboratory measurements of $NO_2 + OH$ suggested by Dransfield et al.[22] is approximately 6% lower than the current JPL 2000 recommendation for the present data set. This difference increases with decreasing temperature, reaching 15% at 200 K, and reasonably reflects the residual uncertainty in the rate constant under stratospheric conditions. Second, the analysis presented here assumes that the $NO_2 + OH$ reaction produces nitric acid with unit yield. This may not be the case. Recently, Golden and Smith[44] and Matheu and Green[45] independently presented theoretical studies suggesting that the HOONO isomer may be a major product of the $NO_2 + OH$ reaction under some conditions. For the conditions typical of the present data set, Golden and Smith[44] predict a yield of nitric acid of only 0.8. Assuming that any HOONO produced is short-lived and returns to NO_x, this yield would effectively reduce L_{NO_x} by 20%. While HOONO has not been observed directly under these conditions,[46] there is strong experimental evidence that the predictions of Golden and Smith[44] are correct at 298 K.[47] Since Cohen et al.[12] found that the ratio of HNO_3 formation through N_2O_5 hydrolysis to the formation through $NO_2 + OH$ is accurate, a 20% change in the rate of $NO_2 + OH$ would also imply an error in the N_2O_5 chemistry.

Through the direct use of in situ measurements and the strict selection criteria, the present analysis provides a highly constrained assessment of the accuracy of NO_x photochemistry; it specifically isolates the system of gas-phase NO_x-HNO_3 exchange processes and minimizes uncertainties introduced by air parcel history, the photochemistry of other chemical systems (e.g., HO_x), and the loss of NO_x through heterogeneous hydrolysis of N_2O_5. In summary, this analysis provides the following context in which to evaluate the NO_x system using a more general approach as is done in the next section:

(1) P_{NO_x}/L_{NO_x} is remarkably consistent, indicating that the present model of NO_x chemistry adequately accounts for the range of conditions observed in this data set;

(2) the fractional contribution of the reaction $HNO_3 + OH$ to total NO_x production (F_{HNO_3+OH}) is invariant throughout the data set; and

(3) R_{NO_2+OH} dominates NO_x loss, indicating that neglecting $R_{BrONO_2+H_2O}$ does not significantly affect the accuracy of the NO_x model.

4. NO_2/HNO_3, F_{HNO_3+OH}, and the $J_{HNO_3}-[OH]$ Relationship

In this section, we examine the general behavior of $[NO_2]_{24h-avg}/[HNO_3]$ in regions of continuous sunlight and the partitioning between the NO_x production processes, R_{HNO_3+OH} and $R_{HNO_3+h\nu}$, throughout the lower stratosphere. Through a simplification of the kinetic equations governing these terms, we show that the partitioning between NO_2 and HNO_3 in this region is predominantly a function of temperature and pressure and that the fractional contribution of R_{HNO_3+OH} to total NO_x production is between 0.4 and 0.6 throughout most of the lower stratosphere. These results are largely a consequence of the strong correlation between the photolysis rate of HNO_3 and the concentration of OH observed throughout the lower stratosphere.

Neglecting the conversion of NO_2 to HNO_3 through $BrONO_2$ hydrolysis, the diurnal steady-state expression for NO_x is

$$\int_{24h} k_{NO_2+OH}[OH][NO_2]\,dt = \int_{24h} (J_{HNO_3} + k_{HNO_3+OH}[OH])[HNO_3]\,dt \quad (7)$$

This expression may be rearranged to solve for $[NO_2]_{24h-avg}/[HNO_3]$:

$$\frac{[NO_2]_{24h-avg}}{[HNO_3]} \cong \frac{\dfrac{\int_{24h} J_{HNO_3}}{\int_{24h}[OH]} + k_{HNO_3+OH}}{\xi k_{NO_2+OH}} \quad (8)$$

where the concentration of HNO_3 is taken to be constant over a 24 h period. The symbol ξ represents a correction factor to account for the difference between the integral of the convolution of OH and NO_2 and the integral of OH multiplied by a 24 h average NO_2 concentration

$$\int_{24h} [OH][NO_2]\,dt = \xi[NO_2]_{24h-avg} \int_{24h} [OH]\,dt \quad (9)$$

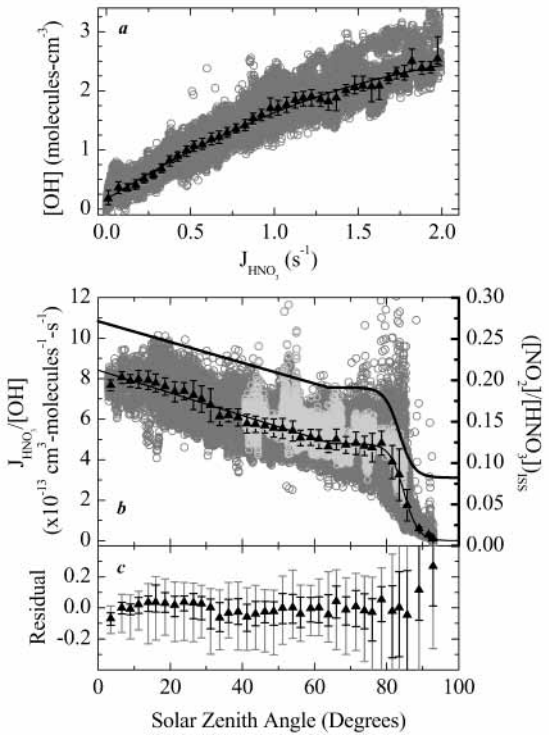

Figure 5. (a) [OH] versus J_{HNO_3} for POLARIS and ASHOE/MAESA measurements satisfying the requirements: $\theta > 400$ K, $T > 195$ K, and SZA < 80° at local noon. $J^{INSITU}_{HNO_3}$ photolysis rates are only available for POLARIS data obtained at SZA<80°. For other data, $J^{SATELLITE}_{HNO_3}$ photolysis rates are used. The median value (▲) and innerquartile range of the measurements are shown for equally spaced intervals along the abscissa. The black line is a least-squares fit of the equation, $[OH] = \alpha J^2_{HNO_3} + \beta J_{HNO_3} + \chi$, to the average values. The parameter values are reported in Table 5. (b) J_{HNO_3}/[OH] versus SZA for the data plotted in (a) with measurements in continuous sunlight differentiated (light gray circles). The median value (▲) and inner-quartile range of the measurements are shown for equally spaced intervals along the abscissa. The thin black line is a fit to the median values using a piecewise continuous function as described in the text. The thick black line is the instantaneous steady-state value of $[NO_2]/[HNO_3]$ at 230 K and 1.73×10^{18} molecules·cm^{-3} (55 mbar). The residuals are plotted in panel c, and the median value (▲) and inner-quartile range of the measurements are shown for equally spaced intervals along the abscissa. The 5th−95th percentile range is also included.

For this data, ξ is 0.96 ± 0.03. Thus, in regions of continuous sunlight, the $[NO_2]_{24h-avg}/[HNO_3]$ ratio is dependent upon the rate constants, k_{NO_2+OH} and k_{HNO_3+OH}, and the relationship between HNO_3 photolysis and the concentration of OH.

Similarly, the fractional contribution of R_{HNO_3+OH} to total NO_x production can be written as

$$F_{HNO_3+OH} = \frac{\int_{24h} k_{HNO_3+OH}[OH]\,dt}{\int_{24h} J_{HNO_3}\,dt + \int_{24h} k_{HNO_3+OH}[OH]\,dt}$$

$$= \frac{k_{HNO_3+OH}}{\frac{\int_{24h} J_{HNO_3}}{\int_{24h}[OH]} + k_{HNO_3+OH}} \qquad (10)$$

and is also dependent upon the term $\int_{24h} J_{HNO_3}/\int_{24h}[OH]$. The concentration of OH is controlled by a large number of processes, making the theoretical relationship between HNO_3 photolysis and the concentration of OH complex;[36] however, the empirical relationship between these terms has been well established with in situ measurements of [OH] from the ER-2.

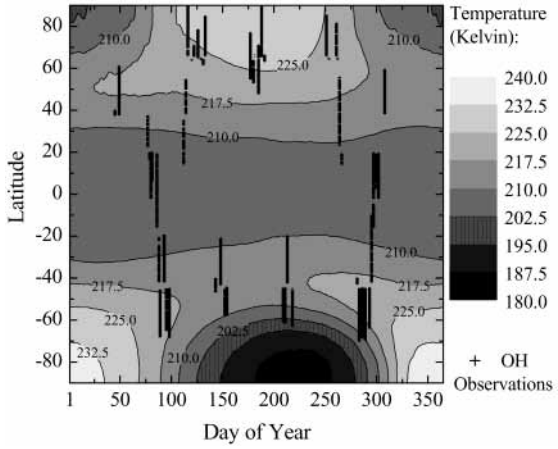

Figure 6. Latitude−day coverage of the OH measurements (+) shown in Figure 5 superimposed on the climatological mean temperatures at 55 mbar.

TABLE 5: J_{HNO_3}−[OH] Relationship

OH vs J_{HNO_3} parabolic fit		J_{HNO_3}/OH functional fit	
α	-3.126×10^{17}	*a*	-5.591×10^{-15}
β	1.748×10^{12}	*b*	8.420×10^{-13}
χ	1.904×10^{5}	*c*	4.852×10^{-13}
		d	83.49
		e	2.025

***J_{HNO_3}* and [OH].** Figure 5a shows measurements of [OH] plotted against calculated HNO_3 photolysis rates for all data obtained during the POLARIS and ASHOE/MAESA ER-2 campaigns. The data are restricted to observations at $\theta > 400$ K. We also require the temperature to exceed 195 K and the SZA at local noon to be less than 80°. $J^{INSITU}_{HNO_3}$ photolysis rates are only available for POLARIS observations at SZA < 80°. For other data, $J^{SATELLITE}_{HNO_3}$ photolysis rates are used. With this large data set (>65 000 measurements), the difference in precision between $J^{INSITU}_{HNO_3}$ and $J^{SATELLITE}_{HNO_3}$ characterized in section 3 should not significantly affect the average relationship between [OH] and J_{HNO_3}. These data have good latitudinal (−70 S to 90 N) and seasonal (mid-February through October) coverage as shown in Figure 6. The observations show a strong, almost linear correlation between the concentration of OH and the photolysis rate of HNO_3. This correlation is well characterized by the equation, $[OH] = \alpha J^2_{HNO_3} + \beta J_{HNO_3} + \chi$, where the parameters are calculated using a least-squares fit to the median values and are reported in Table 5. Figure 5b shows J_{HNO_3}/[OH] as a function of SZA. This ratio varies slowly between the SZA value of 0° to 80°, falling off rapidly at SZA > 80°. At these high sun angles, the photolysis rate of HNO_3 decreases more rapidly than the concentration of OH, which continues to be produced through the photolysis of HNO_4 and HOBr.[48] The SZA dependence of J_{HNO_3}/[OH] is modeled with a piecewise continuous function:

$$\frac{J_{HNO_3}}{[OH]} = a(SZA) + b \quad (SZA < 63.8°)$$

$$\frac{J_{HNO_3}}{[OH]} = \frac{c}{1 + e^{(SZA-d)/e}} \quad (SZA < 63.8°) \qquad (11)$$

where the parameters are calculated using a least-squares fit to the median values and are reported in Table 5. The residuals

(Figure 5c) show that for SZA < 80° nearly 50% of the J_{HNO_3}/[OH] measurements are within 10% of the fit and nearly 90% of the measurements are within 20% of the fit. Observations obtained in the region of continuous sunlight are highlighted and are slightly larger (~10%) on average than the parametrization.

The tight correlation between J_{HNO_3} and [OH] observed throughout the lower stratosphere influences the term, $\int_{24h} J_{HNO_3}/\int_{24h}$[OH]. This term can be equivalently expressed as

$$\frac{\int_{24h} J_{HNO_3}\,dt}{\int_{24h}[OH]\,dt} = \int_{24h} \frac{[OH]}{\int_{24h}[OH]\,dt}\frac{J_{HNO_3}}{[OH]}\,dt \qquad (12)$$

and represents the diurnal average of J_{HNO_3}/[OH] weighted by the instantaneous concentration of OH. The concentration of OH is tightly correlated with SZA throughout the lower stratosphere.[35,36] For the POLARIS and ASHOE/MAESA data shown in Figure 5, the concentration of OH is well approximated by

$$[OH] = 2.9 \times 10^6(94 - SZA)/94 \qquad (13)$$

Combining eqs 11 and 13, $\int_{24h} J_{HNO_3}/\int_{24h}$[OH] can be expressed as a function of SZA only. The value of this term is most strongly influenced by the value of J_{HNO_3}/[OH] near local noon (when [OH] is greatest); thus, the value of $[NO_2]_{24h-avg}/[HNO_3]$ and of F_{HNO_3+OH} is strongly influenced by the noontime conditions.

The parametrization of J_{HNO_3}/[OH] as a function of SZA can be used to calculate the instantaneous steady-state (ISS) value of NO_2/HNO_3, $(NO_2/HNO_3)_{ISS}$, the ratio toward which the NO_x system is driving at a given time of day. Analogous to eq 8, this ratio is equal to $(J_{HNO_3}/[OH] + k_{HNO_3+OH})/k_{NO_2+OH}$ and is included in Figure 5b for representative T and [M] values of 230 K and 1.73×10^{18} molecules·cm^{-3}, or equivalently a pressure of 55 mbar. The shape of J_{HNO_3}/[OH] is reflected in $(NO_2/HNO_3)_{ISS}$, but the percent change in $(NO_2/HNO_3)_{ISS}$ is only about half that of J_{HNO_3}/[OH] because the fractional contribution of J_{HNO_3}/[OH] to the numerator of $(NO_2/HNO_3)_{ISS}$ is only about 60%. From Figure 5b, we conclude that when heterogeneous processes are negligible, the NO_x system is driving toward one value, $[NO_2]/[HNO_3] \sim 0.2$, over a large range in SZA.

Since J_{HNO_3}/[OH] changes slowly for SZA < 80°, increasing by only about 20% between 80° and 40°, air parcels in continuous sunlight conditions that spend a large fraction of the day at SZA < 80° will have nearly constant $\int_{24h} J_{HNO_3}/\int_{24h}$[OH]. For these conditions, eq 8 becomes

$$\frac{[NO_2]_{24h-avg}}{[HNO_3]} \cong \frac{\text{constant} + k_{HNO_3+OH}}{\xi k_{NO_2+OH}} \qquad (14)$$

and the steady-state value of $[NO_2]_{24h-avg}/[HNO_3]$ becomes simply a function of T and [M] determined by the rate constants, k_{NO_2+OH} and k_{HNO_3+OH}. Similarly, eq 10 predicts F_{HNO_3+OH} will be constant as is observed in the measurements (Figure 4b).

$[NO_2]_{24h-avg}/[HNO_3]$ Ratio as a Function of T and [M]. Under conditions of continuous solar illumination, the diurnal behavior of NO_2 and HNO_3 is well understood and the diurnal average NO_2/HNO_3 ratio can be inferred directly from the instantaneous in situ measurements with little increase in uncertainty beyond that of the original measurements; for the POLARIS data, the inferred value of $[NO_2]_{24h-avg}/[HNO_3]$ has a systematic uncertainty of approximately ±22%. These values of $[NO_2]_{24h-avg}/[HNO_3]$ are plotted versus [M] in Figure 7a and provide an opportunity to directly test eq 14. The data reveal a compact relationship between $[NO_2]_{24h-avg}/[HNO_3]$ and [M]. Variation in the temperature history of these measurements is small; mean temperatures along the back trajectory range from 223 to 232 K, with a mean and standard deviation of 230 ± 1 K. At a fixed [M], we expect a 1σ spread of ±0.002 in $[NO_2]_{24h-avg}/[HNO_3]$ as a result of differences in the history of temperature and [M]. With the spread observed in $[NO_2]_{24h-avg}/[HNO_3]$ being roughly ±0.015, the variation due to temperature is too small to detect.

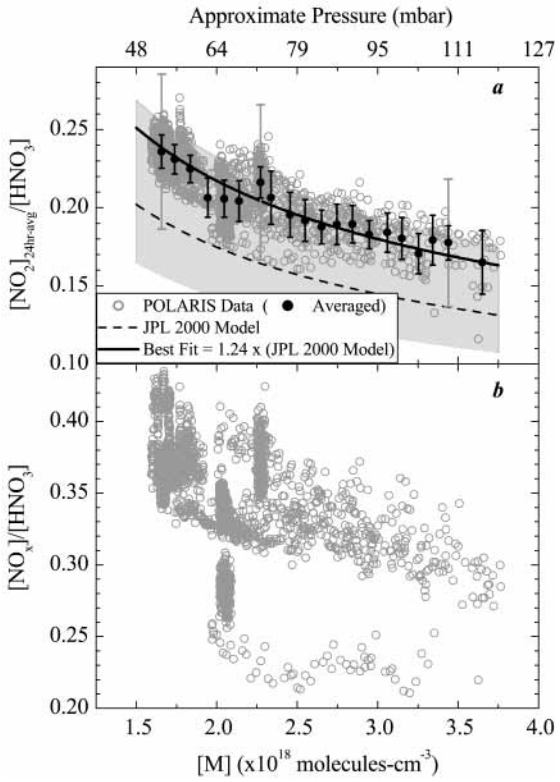

Figure 7. (a) $[NO_2]_{24h-avg}/[HNO_3]$ as a function of [M] for measurements in continuous sunlight where $[NO_2]_{24h-avg}$ is determined from measured NO_x using the effective albedo along the back-trajectory to define the diurnal partitioning between NO and NO_2. The average value (●) and standard deviation of the measurements are shown for equally spaced intervals along the abscissa. The gray error bars represent the estimated total systematic uncertainty. The modeled steady-state $[NO_2]_{24h-avg}/[HNO_3]$ ratio is calculated at 230 K using JPL 2000 (− − −) rate constants and $\int_{24h} J_{HNO_3}/\int_{24h}$[OH] calculated from the $J_{HNO_3}-$[OH] relation established in Figure 5. The gray shading indicates the estimated total systematic uncertainty in this model derived from uncertainties in J_{HNO_3}, OH, k_{NO_2+OH}, and k_{HNO_3+OH}. This shading accounts for the systematic difference in J_{HNO_3}/[OH] observed between the continuous sunlight measurements and the average relation. A least-squares fit to the binned averages of the observations is also shown (—). (b) $[NO_x]/[HNO_3]$ versus [M] for measurements in continuous sunlight.

In Figure 7a, we compare observations of $[NO_2]_{24h-avg}/[HNO_3]$ to the values calculated using eq 8. The expected ratio is calculated for JPL 2000 rate constants evaluated at a temperature of 230 K and in combination with the average value of $\int_{24h} J_{HNO_3}/\int_{24h}$[OH] predicted from eq 12 using the SZA parametrization of J_{HNO_3}/[OH] and [OH] (eqs 11 and 13). For the data in this analysis, the average value of $\int_{24h} J_{HNO_3}/\int_{24h}$[OH] is calculated to be $(4.9 \pm 0.1) \times 10^{-13}$ cm^3·molecule^{-1}·s^{-1}. On average, the measurements of $[NO_2]_{24h-avg}/[HNO_3]$ exceed the model by 24%, larger than the 18% difference expected

from the P_{NO_x}/L_{NO_x} analysis shown in Figure 4a. This discrepancy arises because the average value of $\int_{24h} J_{HNO_3}/\int_{24h}[OH]$ for the continuous sunlight measurements, $(5.4 \pm 0.6) \times 10^{-13}$ cm^3·molecule^{-1}·s^{-1}, is approximately 10% larger than the value predicted using eq 12.

The temperature dependence of $[NO_2]_{24h-avg}/[HNO_3]$ is determined by that of k_{HNO_3+OH} and k_{NO_2+OH}. Both of these rate constants increase with decreasing temperature. Since these reactions are split between production and loss of NO_x, the temperature dependence in the ratio is significantly less than that of the individual reactions. For an increase of 20 K, the percentage change in $[NO_2]_{24h-avg}/[HNO_3]$ transitions from a 7% increase near 1.6×10^{18} molecules·cm^{-3} to almost no change at 3.5×10^{18} molecules·cm^{-3}. For a decrease of 20 K, the percentage change in $[NO_2]_{24h-avg}/[HNO_3]$ transitions from only a 1% increase near 1.6×10^{18} molecules·cm^{-3} to a 13% increase at 3.5×10^{18} molecules·cm^{-3}.

Measurements of $[NO_x]/[HNO_3]$ are plotted versus [M] in Figure 7b. The increase in the spread of the data for fixed values of [M] (relative to Figure 7a) is due entirely to variability in [NO]. NO acts as a reservoir of NO_x that may fluctuate in size without affecting the diurnal average abundance of NO_2; $[NO_2]_{24h-avg}/[HNO_3]$ is determined solely by NO_x-HNO_3 exchange processes. The variability in [NO] is primarily caused by changes in $[O_3]$ that alter the abundance of NO relative to NO_2. The particularly distinct set of data where $[NO_x]/[HNO_3]$ falls below 0.3 originates from the two flights in May (970506 and 970513) where the O_3 levels were higher by 400 to 600 ppb (~20% at [M] = 2×10^{18} molecules·cm^{-3}), reducing the fraction of NO_x present as NO.

Generalizing to a Global Picture. Experimental confirmation of the [M] dependence (at constant T) of $[NO_2]_{24h-avg}/[HNO_3]$ supports the validity of using the simple model described by eq 8 to predict the seasonal evolution of $[NO_2]_{24h-avg}/[HNO_3]$ during polar summer. Rearrangement of eq 8 shows that the diurnal, steady-state value of $[NO_2]_{24h-avg}/[HNO_3]$ is a weighted average of the instantaneous, steady-state $[NO_2]/[HNO_3]$ ratio:

$$\frac{[NO_2]_{24h-avg}}{[HNO_3]} \cong 1.24 \frac{\int_{24h}(J_{HNO_3} + k_{HNO_3+OH}[OH])\,dt}{\xi \int_{24h} k_{NO_2+OH}[OH]\,dt}$$

$$= \frac{1.24}{\xi} \int_{24h} \frac{[OH]}{\int_{24h}[OH]\,dt} \left(\frac{J_{HNO_3} + k_{HNO_3+OH}[OH]}{k_{NO_2+OH}[OH]} \right) dt$$

$$= \frac{1.24}{\xi} \int_{24h} \frac{[OH]}{\int_{24h}[OH]\,dt} \left(\frac{[NO_2]}{[HNO_3]} \right)_{ISS} dt \qquad (15)$$

where the weighting function is the concentration of OH. In this equation, we include a correction factor of 1.24 to account for the discrepancy between measured and modeled $[NO_2]_{24h-avg}/[HNO_3]$ shown in Figure 7a. The value of $[NO_2]_{24h-avg}/[HNO_3]$ is primarily determined by the instantaneous, steady-state $[NO_2]/[HNO_3]$ ratio near local noon when the concentration of OH is greatest and the instantaneous time constant for the NO_x system is shortest.

Both the concentration of OH and the value of $([NO_2]/[HNO_3])_{ISS}$ are well parametrized as functions of SZA. The parametrizations for [OH] and $([NO_2]/[HNO_3])_{ISS}$ are presented in eq 13 and Figure 5, respectively.

For continuous sunlight conditions, $[NO_2]_{24h-avg}/[HNO_3]$ may be estimated given temperature, [M], and the daily function of SZA defined by latitude and day of year. The latitudinal and seasonal behavior of the diurnal steady-state $[NO_2]_{24h-avg}/[HNO_3]$ ratio derived from this approximation is shown in Figure 8 for zonally averaged temperatures on the 55 mbar pressure surface (Figure 6). This mapping of $[NO_2]_{24h-avg}/[HNO_3]$ is consistent with the in situ measurements obtained from the ER-2. The uncertainty in this ratio is approximated by the estimated systematic uncertainty (±22%, 1σ) in the measured values of $[NO_2]_{24h-avg}/[HNO_3]$.

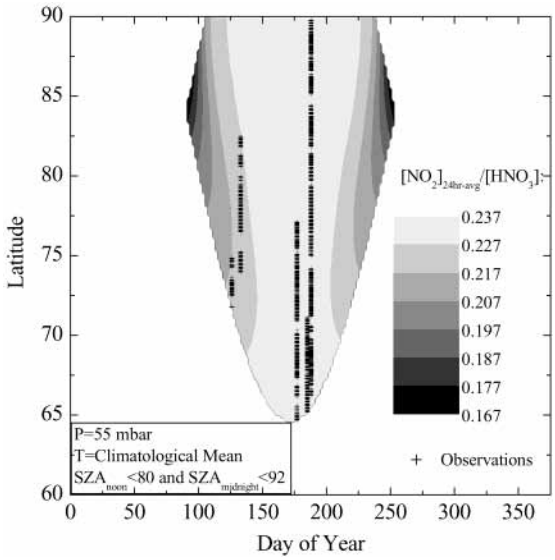

Figure 8. Modeled behavior of steady-state $[NO_2]_{24h-avg}/[HNO_3]$ in the region of continuous sunlight. $[NO_2]_{24h-avg}/[HNO_3]$ is estimated using eq 15 with the climatological mean temperature at 55 mbar shown in Figure 6. The calculations are restricted to regions where the SZA at local midnight is less than 92° and at local noon is less than 80°.

In a similar analysis, the fractional contribution of HNO_3 reaction with OH to total NO_x production integrated over the day may be expressed as

$$F_{HNO_3+OH} = \frac{k_{HNO_3+OH}}{\int_{24h} \frac{[OH]}{\int_{24h}[OH]\,dt} \frac{J_{HNO_3}}{[OH]}\,dt + k_{HNO_3+OH}} \qquad (16)$$

where we observe that the 24 h average partitioning is also weighted by the concentration of OH. In contrast to eq 15, this calculation does not require continuous sunlight conditions and is generally applicable throughout most of the lower stratosphere. Thus, with both $J_{HNO_3}/[OH]$ and [OH] parametrized as a function of SZA, the partitioning between the two NO_x production processes, $R_{HNO_3+h\nu}$ and R_{HNO_3+OH}, may be estimated given the temperature and pressure dependence of k_{HNO_3+OH} and the daily function of SZA defined by latitude and day of year. In Figure 9, we present the calculated distribution of F_{HNO_3+OH} on the 55 mbar pressure surface. For these calculations, we require the noontime SZA to be less than 80°. This requirement guarantees that the partitioning between R_{HNO_3+OH} and $R_{HNO_3+h\nu}$ is mostly determined by the relationship between J_{HNO_3} and [OH] where it is well constrained by measurements (at SZA < 85°) as seen in Figure 5.

In Figure 9, we see that throughout most of the day-latitude phase space, the partitioning between the two NO_x production processes is close to 50:50. In regions where the temperatures are cold and the sun remains low in the sky (e.g., near the polar winters), the fractional contribution of R_{HNO_3+OH} to the production of NO_x increases because k_{HNO_3+OH} increases and the [OH]-

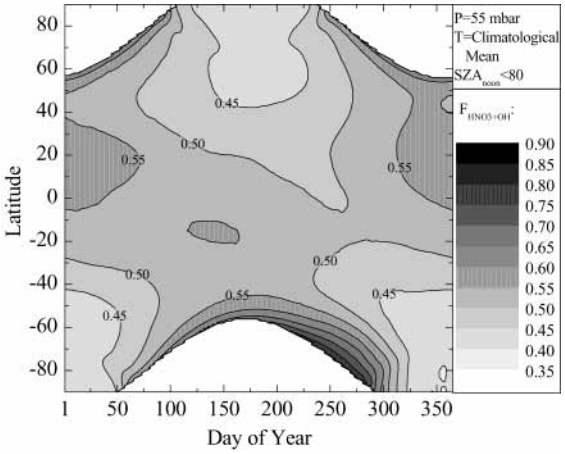

Figure 9. Modeled behavior of the fractional contribution of HNO_3 + OH to total NO_x production as a function of season and latitude. The fractional contribution is estimated using eq 16 and the climatological mean temperature at 55 mbar. The calculations are restricted to regions where the noontime SZA is less than 80°.

weighted average of $J_{HNO_3}/[OH]$ is lower than for most other regions. In the polar summer, the warmer temperatures decrease k_{HNO_3+OH} with a corresponding decrease in the fractional contribution of R_{HNO_3+OH}.

The results presented in Figures 8 and 9 provide a valuable benchmark of the magnitude and character of $[NO_2]_{24h-avg}/[HNO_3]$ and F_{HNO_3+OH} which may be used for evaluating the accuracy of complex 2D and 3D chemical transport models and for comparing observations obtained by different platforms. A significant deviation from these results indicates that the relative value of J_{HNO_3} to the concentration of OH is not well represented in the model. An error of this sort will not only affect the modeled abundance of NO_x, but may also significantly impact halogen chemistry through the coupling with NO_x and/or through the influence of OH on the partitioning of chlorine between $ClONO_2$ and HCl. Furthermore, these errors could compound to influence the calculated O_3 loss rates and the modeled impact of chemical or dynamical perturbations.

5. Conclusions

The set of reactions controlling the partitioning between NO_2 and HNO_3 in the lower stratosphere is greatly simplified in the presence of continuous sunlight, where NO_x-HNO_3 exchange is dominated only by the gas-phase reactions, $R_{HNO_3+h\nu}$, R_{HNO_3+OH}, and R_{NO_2+OH}. Simultaneous observations of NO_x and HO_x radicals, their precursors, and the radiation field obtained from the NASA ER-2 aircraft during the 1997 POLARIS campaign are used in a detailed analysis to characterize the NO_x-HNO_3 system in this region. Through calculations of NO_x production and loss rates constrained by these in situ measurements, we find that the system is precisely and accurately represented by the photochemical model when the effective albedo (a historical average albedo), in situ based determination of overhead O_3, and measured OH are used. Reaction rate constants recommended in the JPL 1997 compendium[17] with updates provided in the JPL 2000 supplement[25] result in NO_x loss exceeding production by 18%, or equivalently, measurements of NO_2 exceeding model calculations by 18%. This analysis reveals a remarkably constant partitioning between the NO_x production processes [R_{HNO_3+OH}, (41 ± 2)%; $R_{HNO_3+h\nu}$, (59 ± 2)%] and confirms that R_{NO_2+OH} dominates NO_x loss, accounting for 95% of NO_x to HNO_3 conversion except near the lowest altitudes.

$[NO_2]_{24h-avg}/[HNO_3]$ inferred directly from in situ NO_2 and NO_y measurements is shown to be only a function of [M], with a value of ~0.23 at 55 mbar. Using the results of these detailed analyses together with a general steady-state description of the NO_x-HNO_3 system, we find that the NO_x-HNO_3 system is controlled by the relationship between the photolysis rate of HNO_3 and the concentration of OH and that the behavior of the system is greatly simplified by the tight correlation between these terms in the lower stratosphere. Characterizing the functional dependence of $J_{HNO_3}/[OH]$ and [OH] on SZA, we develop a fully parameterized description of the NO_x-HNO_3 system which predicts the observed features—the simple dependence of $[NO_2]_{24h-avg}/[HNO_3]$ on [M] and the invariance in the partitioning between the NO_x production processes.

This analysis provides a new perspective on the behavior of NO_x in the lower stratosphere. That atmospheric processes should conspire to produce the tight correlation observed between J_{HNO_3} and OH is not obvious, but knowledge of its existence is a tool to be exploited. This correlation simplifies the relationship among the gas-phase NO_x-HNO_3 exchange processes and fixes the concentration of the NO_2 radical in regions of continuous sunlight, defining the baseline from which the atmosphere will respond to natural or anthropogenic perturbations. In addition, the correlation applies equally to the gas-phase reactions underlying the NO_x-HNO_3 system in regions where heterogeneous reactions constitute a dominant loss process. We provide new diagnostics useful in the intercomparison of measurements and the assessment of uncertainties within 2D and 3D chemical-transport models, including an average distribution of $[NO_2]_{24h-avg}/[HNO_3]$ in the region of continuous sunlight and a mapping of the fractional contribution of HNO_3 + OH to total NO_x production throughout most of the lower stratosphere.

Acknowledgment. We thank the NASA Upper Atmospheric Research Program and Atmospheric Effects of Aviation Project for supporting the POLARIS field campaign. The development of the new $ClO/ClONO_2/NO_2$ instrument was supported by the NASA Upper Atmospheric Research Program and Environmental Research Aircraft and Sensor Technology programs. K.K.P. gratefully acknowledges a graduate fellowship from NSF. We also thank P. A. Newman, L. R. Lait, and M. R. Schoberl for providing the back-trajectory calculations, C. R. Webster for providing N_2O^{ALIAS}, J. C. Wilson for providing aerosol surface area density, and E. R. Nash for providing the climatological mean temperatures. Lastly, we thank N. M. Donahue for his useful input on this manuscript.

References and Notes

(1) Crutzen, P. J. *Q. J. R. Meteorol. Soc.* **1970**, *96*, 320−325.
(2) Johnston, H. *Science* **1971**, *173*, 517−522.
(3) Stimpfle, R. M.; Koplow, J. P.; Cohen, R. C.; Kohn, D. W.; Wennberg, P. O.; Judah, D. M.; Toohey, D. W.; Avallone, L. M.; Anderson, J. G.; Salawitch, R. J.; Woodbridge, E. L.; Webster, C. R.; May, R. D.; Proffitt, M. H.; Aiken, K.; Margitan, J.; Loewenstein, M.; Podolske, J. R.; Pfister, L.; Chan, K. R. *Geophys. Res. Lett.* **1994**, *21*, 2543−6.
(4) Dessler, A. E.; Kawa, S. R.; Douglass, A. R.; Considine, D. B.; Kumer, J. B.; Roche, A. E.; Mergenthaler, J. L.; Waters, J. W.; Russell, J. M., III; Gille, J. C. *J. Geophys. Res.* **1996**, *101*, 12515−21.
(5) Stimpfle, R. M.; Cohen, R. C.; Bonne, G. P.; Voss, P. B.; Perkins, K. K.; Koch, L. C.; Anderson, J. G.; Salawitch, R. J.; Lloyd, S. A.; Gao, R. S.; Del Negro, L. A.; Keim, E. R.; Fahey, D. W.; Proffitt, M. H.; Bui, T. P. *J. Geophys. Res.* **1999**, *104*, 26705−14.
(6) Cohen, R. C.; Wennberg, P. O.; Stimpfle, R. M.; Koplow, J.; Anderson, J. G.; Fahey, D. W.; Woodbridge, E. L.; Keim, E. R.; Gao, R.; Proffitt, M. H.; Loewenstein, M.; Chan, K. R. *Geophys. Res. Lett.* **1994**, *21*, 2539−42.
(7) Lanzendorf, E. J.; Hanisco, T. F.; Stimpfle, R. M.; Anderson, J. G.; Wennberg, P. O.; Cohen, R. C.; Gao, R. S.; Margitan, J. J.; Bui, T. P. *J. Phys. Chem. A* **2001**, *105*, 1535−1542.

(8) Gao, R. S.; Fahey, D. W.; Salawitch, R. J.; Lloyd, S. A.; Anderson, D. E.; DeMajistre, R.; McElroy, C. T.; Woodbridge, E. L.; Wamsley, R. C.; Donnelly, S. G.; Del Negro, L. A.; Proffitt, M. H.; Stimpfle, R. M.; Kohn, D. W.; Kawa, S. R.; Lait, L. R.; Loewenstein, M.; Podolske, J. R.; Keim, E. R.; Dye, J. E.; Wilson, J. C.; Chan, K. R. *J. Geophys. Res.* **1997**, *102*, 3935−49.

(9) Morris, G. A.; Considine, D. B.; Dessler, A. E.; Kawa, S. R.; Kumer, J.; Mergenthaler, J.; Roche, A.; Russell, J. M., III *J. Geophys. Res.* **1997**, *102*, 8955−65.

(10) Slusser, J.; Liu, X.; Stamnes, K.; Shaw, G.; Smith, R.; Storvold, R.; Murcray, F.; Lee, A.; Good, P. *J. Geophys. Res.* **1998**, *103*, 1549−54.

(11) Sen, B.; Toon, G. C.; Osterman, G. B.; Blavier, J. F.; Margitan, J. J.; Salawitch, R. J.; Yue, G. K. *J. Geophys. Res.* **1998**, *103*, 3571−85.

(12) Cohen, R. C.; Perkins, K. K.; Koch, L. C.; Stimpfle, R. M.; Wennberg, P. O.; Hanisco, T. F.; Lanzendorf, E. J.; Bonne, G. P.; Voss, P. B.; Salawitch, R. J.; Del Negro, L. A.; Wilson, J. C.; McElroy, C. T.; Bui, T. P. *J. Geophys. Res.*, **2000**, *105*, 24283−24304.

(13) Mozurkewich, M.; Calvert, J. G. *J. Geophys. Res.* **1988**, *93*, 15889−96.

(14) McElroy, M. B.; Salawitch, R. J.; Minschwaner, K. *Planet. Space Sci.* **1992**, *40*, 373−401.

(15) Fahey, D. W.; Kawa, S. R.; Woodbridge, E. L.; Tin, P.; Wilson, J. C.; Jonsson, H. H.; Dye, J. E.; Baumgardner, D.; Borrmann, S.; Toohey, D. W.; Avallone, L. M.; Proffitt, M. H.; Margitan, J.; Loewenstein, M.; Podolske, J. R.; Salawitch, R. J.; Wofsy, S. C.; Ko, M. K. W.; Anderson, D. E.; Schoeberl, M. R.; Chan, K. R. *Nature* **1993**, *363*, 509−14.

(16) Singh, H.; Chen, Y.; Tabazadeh, A.; Fukui, Y.; Bey, I.; Yantosca, R.; Jacob, D.; Arnold, F.; Wohlfrom, K.; Atlas, E.; Flocke, F.; Blake, D.; Blake, N.; Heikes, B.; Snow, J.; Talbot, R.; Gregory, G.; Sachse, G.; Vay, S.; Kondo, Y. *J. Geophys. Res.* **2000**, *105*, 3795−3805.

(17) DeMore, W. B.; Sander, S. P.; Golden, D. M.; Hampson, R. F.; Kurylo, M. J.; Howard, C. J.; Ravishankara, A. R.; Kolb, C. E.; Molina, M. J. JPL Publication 97-4, 1997.

(18) Gao, R. S.; Fahey, D. W.; Del Negro, L. A.; Donnelly, S. G.; Keim, E. R.; Neuman, J. A.; Teverovski, E.; Wennberg, P. O.; Hanisco, T. F.; Lanzendorf, E. J.; Proffitt, M. H.; Margitan, J. J.; Wilson, J. C.; Elkins, J. W.; Stimpfle, R. M.; Cohen, R. C.; McElroy, C. T.; Bui, T. P.; Salawitch, R. J.; Brown, S. S.; Ravishankara, A. R.; Portmann, R. W.; Ko, M. K. W.; Weisenstein, D. K.; Newman, P. A. *Geophys. Res. Lett.* **1999**, *26*, 1153−1156.

(19) Jucks, K. W.; Johnson, D. G.; Chance, K. V.; Traub, W. A.; Margitan, J. J.; Salawitch, R. J. *J. Geophys. Res.* **1999**, *104*, 26715−23.

(20) Osterman, G. B.; Sen, B.; Toon, G. C.; Salawitch, R. J.; Margitan, J. J.; Blavier, J. F.; Fahey, D. W.; Gao, R. S. *Geophys. Res. Lett.* **1999**, *26*, 1157−1160.

(21) Pierson, J. M.; Kawa, S. R.; Salawitch, R. J.; Hanisco, T. F.; Lanzendorf, E. J.; Perkins, K. K.; Gao, R. S.; Cohen, R. C. *J. Geophys. Res.* **2000**, *105*, 15185−15199.

(22) Dransfield, T. J.; Perkins, K. K.; Donahue, N. M.; Anderson, J. G.; Sprengnether, M. M.; Demerjian, K. L. *Geophys. Res. Lett.* **1999**, *26*, 687−690.

(23) Brown, S. S.; Talukdar, R. K.; Ravishankara, A. R. *Chem. Phys. Lett.* **1999**, *299*, 277−84.

(24) Brown, S. S.; Talukdar, R. K.; Ravishankara, A. R. *J. Phys. Chem.* **1999**, *103*.

(25) Sander, S. P.; Friedl, R. R.; DeMore, W. B.; Golden, D. M.; Kurylo, M. J.; Hampson, R. F.; Huie, R. E.; Moortgat, G. K.; Ravishankara, A. R.; Kolb, C. E.; Molina, M. J. JPL Publication 00-3, 2000.

(26) Wofsy, S. C.; Cohen, R. C.; Schmeltekopf, A. L. *Geophys. Res. Lett.* **1994**, *21*, 2535−8.

(27) Tuck, A. F.; Brune, W. H.; Hipskind, R. S. *J. Geophys. Res.* **1997**, *102*, 3901−3904.

(28) Perkins, K. K. In Situ Observations of Nitrogen Dioxide using Laser-Induced Fluorescence Detection: Examining the NO_2-HNO_3 System in the Lower Stratosphere. Ph.D. Thesis, Harvard University, 2000.

(29) Bonne, G. P. In Situ Measurements of Chlorine Nitrate in the Lower Stratosphere. Ph.D. Thesis, Harvard University, 1998.

(30) Del Negro, L. A.; Fahey, D. W.; Gao, R. S.; Donnelly, S. G.; Keim, E. R.; Neuman, J. A.; Cohen, R. C.; Perkins, K. K.; Koch, L. C.; Salawitch, R. J.; Lloyd, S. A.; Proffitt, M. H.; Margitan, J. J.; Stimpfle, R. M.; Bonne, G. P.; Voss, P. B.; Hanisco, T. F.; Lanzendorf, E. J.; Wennberg, P. O.; McElroy, C. T.; Newman, P. A.; Lait, L. R.; Bui, T. P. *J. Geophys. Res.* **1999**, *104*, 26687−703.

(31) Gao, R. S.; Keim, E. R.; Woodbridge, E. L.; Ciciora, S. J.; Proffitt, M. H.; Thompson, T. L.; McLaughlin, R. J.; Fahey, D. W. *J. Geophys. Res.* **1994**, *99*, 20673−81.

(32) Prather, M. J. *J. Geophys. Res.* **1981**, *86*, 5325−38.

(33) Salawitch, R. J.; Wofsy, S. C.; Wennberg, P. O.; Cohen, R. C.; Anderson, J. G.; Fahey, D. W.; Gao, R. S.; Keim, E. R.; Woodbridge, E. L.; Stimpfle, R. M.; Koplow, J. P.; Kohn, D. W.; Webster, C. R.; May, R. D.; Pfister, L.; Gottlieb, E. W.; Michelsen, H. A.; Yue, G. K.; Wilson, J. C.; Brock, C. A.; Jonsson, H. H.; Dye, J. E.; Baumgardner, D.; Proffitt, M. H.; Loewenstein, M.; Podolske, J. R.; Elkins, J. W.; Dutton, G. S.; Hintsa, E. J.; Dessler, A. E.; Weinstock, E. M.; Kelly, K. K.; Boering, K. A.; Daube, B. C.; Chan, K. R.; Bowen, S. W. *Geophys. Res. Lett.* **1994**, *21*, 2547−50.

(34) Michelsen, H. A.; Salawitch, R. J.; Wennberg, P. O.; Anderson, J. G. *Geophys. Res. Lett.* **1994**, *21*, 2227−30.

(35) Wennberg, P. O.; Cohen, R. C.; Stimpfle, R. M.; Koplow, J. P.; Anderson, J. G.; Salawitch, R. J.; Fahey, D. W.; Woodbridge, E. L.; Keim, E. R.; Gao, R. S.; Webster, C. R.; May, R. D.; Toohey, D. W.; Avallone, L. M.; Proffitt, M. H.; Loewenstein, M.; Podolske, J. R.; Chan, K. R.; Wofsy, S. C. *Science* **1994**, *266*, 398−404.

(36) Hanisco, T. F.; Lanzendorf, E. J.; Perkins, K. K.; Stimpfle, R. M.; Voss, P. B.; Anderson, J. G.; Wennberg, P. O.; Cohen, R. C.; Fahey, D. W.; Gao, R. S.; Hintsa, E. J.; Salawitch, R. J.; Margitan, J. J.; McElroy, C. T.; Midwinter, C. *J. Phys. Chem. A* **2001**, *105*, 1543−1553.

(37) Wamsley, P. R.; Elkins, J. W.; Fahey, D. W.; Dutton, G. S.; Volk, C. M.; Myers, R. C.; Montzka, S. A.; Butler, J. H.; Clarke, A. D.; Fraser, P. J.; Steele, L. P.; Lucarelli, M. P.; Atlas, E. L.; Schauffler, S. M.; Blake, D. R.; Rowland, F. S.; Sturges, W. T.; Lee, J. M.; Penkett, S. A.; Engel, A.; Stimpfle, R. M.; Chan, K. R.; Weisenstein, D. K.; Ko, M. K. W.; Salawitch, R. J. *J. Geophys. Res.* **1998**, *103*, 1513−26.

(38) Swartz, W. H.; Lloyd, S. A.; Kusterer, T. L.; Anderson, D. E.; McElroy, C. T.; Midwinter, C. *J. Geophys. Res.* **1999**, *104*, 26725−35.

(39) Fahey, D. W.; Gao, R. S.; Del Negro, L. A.; Keim, E. R.; Kawa, S. R.; Salawitch, R. J.; Wennberg, P. O.; Hanisco, T. F.; Lanzendorf, E. J.; Perkins, K. K.; Lloyd, S. A.; Swartz, W. H.; Proffitt, M. H.; Margitan, J. J.; Wilson, J. C.; Stimpfle, R. M.; Cohen, R. C.; McElroy, C. T.; Webster, C. R.; Loewenstein, M.; Elkins, J. W.; Bui, T. P. *Geophys. Res. Lett.* **2000**, *27*, 2605−2608.

(40) Voss, P. B.; Stimpfle, R. M.; Cohen, R. C.; Hanisco, T. F.; Bonne, G. P.; Perkins, K. K.; Koch, L. C.; Lanzendorf, E. J.; Anderson, J. G.; Webster, C. R.; Scott, D. C.; May, R. D.; Wennberg, P. O.; Salawitch, R. J.; Margitan, J. J.; Gao, R. S.; Bui, T. P.; Newman, P. A.; Lait, L. R. *J. Geophys. Res.*, in press.

(41) Keating, G. M.; Young, D. F. Interim reference ozone models for the middle atmosphere. In *Handbook for MAP*; Labitzke, K., Barnett, J. J., Edwards, B., Eds.; University of Illinois: Urbana, 1985; Vol. 16; p 205−229.

(42) McElroy, C. T. *Geophys. Res. Lett.* **1995**, *22*, 1361−4.

(43) Hanson, D. R.; Ravishankara, A. R.; Lovejoy, E. R. *J. Geophys. Res.* **1996**, *101*, 9063−9.

(44) Golden, D. M.; Smith, G. *J. Phys. Chem.* **2000**, *104*, 3391.

(45) Matheu, D.; Green, W. *Int. J. Chem. Kinet.* **2000**, *32*, 245.

(46) Dransfield, T.; Donahue, N.; Anderson, J. *J. Phys. Chem. A* **2001**, *105*, 1507−1514.

(47) Donahue, N. M.; Dubey, M. K.; Mohrschladt, R.; Dransfield, T. J.; Anderson, J. G. *J. Phys. Chem. A*, submitted for publication.

(48) Wennberg, P. O.; Salawitch, R. J.; Donaldson, D. J.; Hanisco, T. F.; Lanzendorf, E. J.; Perkins, K. K.; Lloyd, S. A.; Vaida, V.; Gao, R. S.; Hintsa, E. J.; Cohen, R. C.; Swartz, W. H.; Kusterer, T. L.; Anderson, D. E. *Geophys. Res. Lett.* **1999**, *26*, 1373−1376.

(49) Fahey, D. W.; Murphy, D. M.; Kelly, K. K.; Ko, M. K. W.; Proffitt, M. H.; Eubank, C. S.; Ferry, G. V.; Loewenstein, M.; Chan, K. R. *J. Geophys. Res.* **1989**, *94*, 16665−81.

(50) Wennberg, P. O.; Cohen, R. C.; Hazen, N. L.; Lapson, L. B.; Allen, N. T.; Hanisco, T. F.; Oliver, J. F.; Lanham, N. W.; Demusz, J. N.; Anderson, J. G. *Rev. Sci. Instrum.* **1994**, *65*, 1858−76.

(51) Hintsa, E. J.; Weinstock, E. M.; Anderson, J. G.; May, R. D.; Hurst, D. F. *J. Geophys. Res.* **1999**, *104*, 8183−8189.

(52) Proffitt, M. H.; McLaughlin, R. J. *Rev. Sci. Instrum.* **1983**, *54*, 1719−28.

(53) Podolske, J.; Loewenstein, M. *Appl. Opt.* **1993**, *32*, 5324−33.

(54) Webster, C. R.; May, R. D.; Trimble, C. A.; Chave, R. G.; Kendall, J. *Appl. Opt.* **1994**, *33*, 454−72.

(55) Scott, S. G.; Paul Bui, T.; Roland Chan, K.; Bowen, S. W. *J. Atmos. Ocean. Technol.* **1990**, *7*, 525−40.

(56) Jonsson, H. H.; Wilson, J. C.; Brock, C. A.; Knollenberg, R. G.; Newton, R.; Dye, J. E.; Baumgardner, D.; Borrmann, S.; Ferry, G. V.; Pueschel, R.; Woods, D. C.; Pitts, M. C. *J. Atmos. Ocean. Technol.* **1995**, *12*, 115−29.